

¹ Susceptible host dynamics explain pathogen resilience to
² perturbations

⁴
⁵ Sang Woo Park, . . . , Sarah Cobey

⁶ Abstract

⁷ Major priority for epidemiological research in the time of anthropogenic change is
⁸ understanding how infectious disease dynamics respond to perturbations. Interven-
⁹ tions to slow the spread of SARS-CoV-2 significantly disrupted the transmission
¹⁰ of other human pathogens. As interventions lifted, whether and when respiratory
¹¹ pathogens would eventually return to their pre-pandemic dynamics remains to be
¹² answered. To address this gap, we develop a framework for estimating pathogen re-
¹³ silience based on how fast epidemic patterns return to their pre-pandemic, endemic
¹⁴ dynamics. Our analysis suggests that some pathogens may have settled to endemic
¹⁵ cycles that are different from their pre-pandemic patterns. Finally, we show that
¹⁶ the replenishment rate of the susceptible pool is a key determinant of pathogen re-
¹⁷ silience. Our framework offers a novel perspective to characterizing the dynamics of
¹⁸ endemic pathogens and their responses to SARS-CoV-2 interventions. [SWP: Need
¹⁹ to emphasize broader implications.]

Non-pharmaceutical interventions (NPIs) to slow the spread of SARS-CoV-2 disrupted the transmission of other human respiratory pathogens, adding uncertainties to their future epidemic dynamics and the overall public health burden [1]. As interventions lifted, large heterogeneities in outbreak dynamics were observed across different pathogens in different countries, with some pathogens exhibiting earlier resurgences than others [2, 3, 4]. Heterogeneities in the overall reduction in transmission and the timing of re-emergence likely reflect differences in NPI patterns, pathogen characteristics, immigration/importation from other countries, and pre-pandemic pathogen dynamics [5]. Therefore, comparing the differential impact of the pandemic NPIs across pathogens can provide unique opportunities to learn about underlying pathogen characteristics, such as their transmissibility or duration of immunity, from heterogeneities in re-emergence patterns [6].

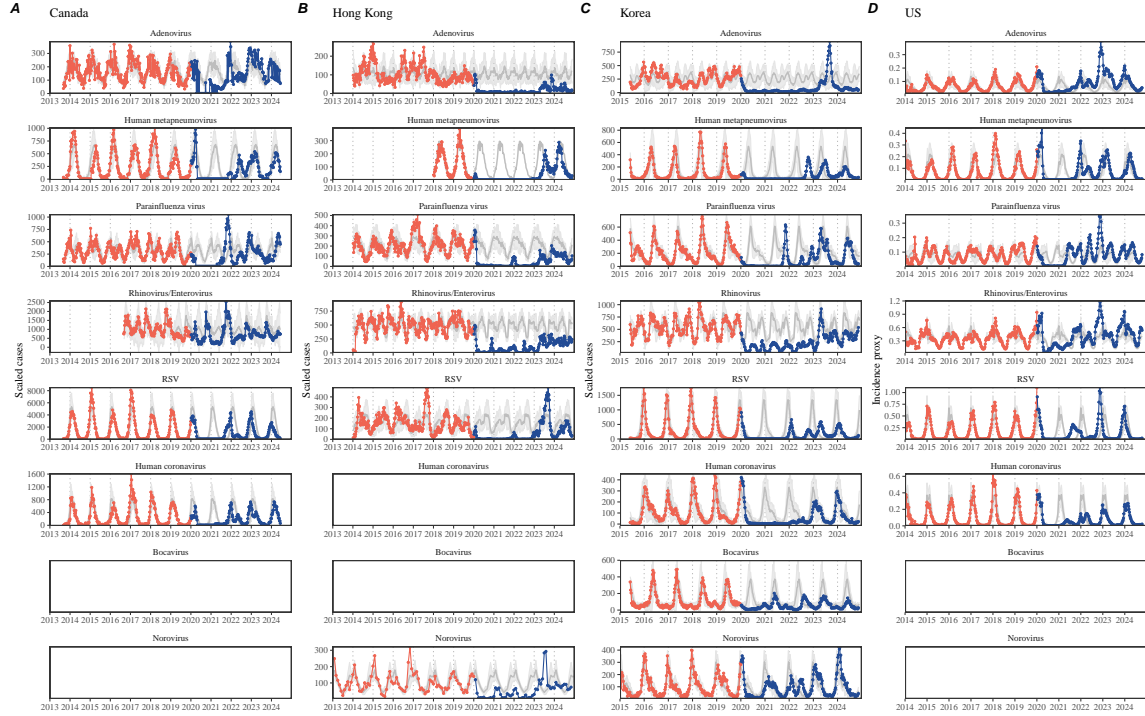


Figure 1: Observed heterogeneity in responses to COVID-19 pandemic across respiratory pathogens and norovirus in (A) Canada, (B) Hong Kong, (C) Korea, and (D) US. Red points and lines represent data before 2020. Blue points and lines represent data since 2020. Gray lines and shaded regions represent the mean seasonal patterns and corresponding 95% confidence intervals around the mean. Mean seasonal patterns were calculated by aggregating cases before 2020 into 52 weekly bins and taking the average in each week. Cases were scaled to account for changes in testing patterns (Materials and Methods).

Even though more than five years have passed since the emergence of SARS-CoV-2, we still observe persistent changes in pathogen dynamics following the pandemic

³⁴ NPIs: for example, compared to pre-pandemic, seasonal patterns, human metapneumovirus and bocavirus in Korea are circulating at lower levels, whereas RSV in Korea
³⁵ seem to exhibit different seasonality (Figure 1). These observations suggest a possibility
³⁶ for a fundamental change in pathogen dynamics following the pandemic NPIs,
³⁷ which can be driven by permanent shift in either human behavior or population-level
³⁸ immunity [7, 8]. Moreover, the possibility of a long-lasting impact of the pandemic
³⁹ NPIs pose an important question for future infectious disease dynamics: can we pre-
⁴⁰ dict whether and when other respiratory pathogens will eventually return to their
⁴¹ pre-pandemic dynamics?

⁴² So far, the majority of epidemiological analyses of respiratory pathogens in the
⁴³ context of the pandemic NPIs have focused on characterizing the timing of rebound
⁴⁴ [1, 9, 5]. Instead, we seek to characterize how fast a pathogen returns to its pre-
⁴⁵ pandemic dynamics. These two concepts have subtle but important differences: for
⁴⁶ example, it took more than 3 years for human metapneumovirus to rebound in Hong
⁴⁷ Kong but the observed epidemic patterns in 2024 are similar to pre-pandemic seasonal
⁴⁸ means, suggesting a rapid return to pre-pandemic dynamics following a perturbation
⁴⁹ (Figure 1). Measuring this rate of return is particularly useful because it allows us
⁵⁰ to quantify the ecological resilience of a host-pathogen system [10, 11, 12, 13].

⁵¹ In this study, we lay out theoretical and statistical approaches to characterizing
⁵² the resilience of a host-pathogen system based on how fast the system recovers from
⁵³ perturbation. We begin by laying out a few representative scenarios that capture
⁵⁴ the potential impact of COVID-19 interventions on endemic pathogen dynamics and
⁵⁵ illustrate how resilience can be measured by comparing the pre- and post-pandemic
⁵⁶ dynamics of susceptible and infected hosts. In practice, information on susceptible
⁵⁷ hosts is often unavailable, making this theoretical approach infeasible. Instead, we
⁵⁸ utilize a mathematical technique to reconstruct empirical attractors from the data
⁵⁹ [14], which allows us to measure the rate at which the host-pathogen system ap-
⁶⁰ proaches this empirical attractor after a perturbation; this rate corresponds to the
⁶¹ resilience of the host-pathogen system. We use this method to analyze pathogen
⁶² surveillance data for respiratory and non-respiratory pathogens from Canada, Hong
⁶³ Kong, Korea, and US. Finally, we show that susceptible host dynamics explain vari-
⁶⁴ ation in pathogen resilience.

⁶⁶ Conceptual introduction to pathogen resilience

⁶⁷ In classical ecological literature, resilience of an ecological system is measured by
⁶⁸ the rate at which the system returns to its reference state following a perturbation
⁶⁹ [10, 11, 12, 13]. This rate corresponds to the largest real part of the eigenvalues of
⁷⁰ the linearized system near equilibrium—here, we refer to this value as the *intrinsic*
⁷¹ resilience of the system, which represents the expected rate of return from perturbed
⁷² states. However, respiratory pathogens often exhibit seasonal variation in transmis-
⁷³ sion, meaning that the intrinsic resilience of a host-pathogen system varies across

74 season. Nonetheless, we can still measure the *empirical* resilience of a host-pathogen
75 system by looking at how fast the system returns to the pre-pandemic, endemic
76 dynamics after interventions are lifted.

77 As an example, we begin with a simple Susceptible-Infected-Recovered-Susceptible
78 (SIRS) model with seasonally forced transmission and demography (i.e., birth and
79 death). The SIRS model is the simplest model that allows for waning of immunity
80 and is commonly used for modeling the dynamics of respiratory pathogens [15]. First,
81 consider an intervention that reduce transmission by 50% for 6 months starting in
82 2020, which causes epidemic patterns to deviate from its original stable annual cycle
83 for a short period of time and eventually come back (Figure 2A). To measure the
84 resilience of this system empirically, we first need to be able to measure the distance
85 from its pre-pandemic attractor. There are many ways we can measure the distance
86 from attractor, but for illustrative purposes, we choose one of the most parsimonious
87 approach: that is, we look at how the susceptible (S) and infected (I) populations
88 change over time and measure the distance on the SI phase plane (Figure 2B). In this
89 simple case, the locally estimated scatterplot smoothing (LOESS) fit indicates that
90 the distance from attractor decreases exponentially (linearly on a log scale) on aver-
91 age (Figure 2C). Furthermore, the overall rate of return approximates the intrinsic
92 resilience of the seasonally unforced system (Figure 2C).

93 Alternatively, NPIs can have a lasting impact on the pathogen dynamics; as an
94 example, we consider a scenario in which a 10% reduction in transmission persists
95 even after the NPIs are lifted (Figure 2D–F). In such cases in practice, we can-
96 not know whether the pathogen will return to its original cycle or a different cycle
97 until many years have passed, and we cannot measure the distance to the new un-
98 known attractor that the system might eventually approach. Nonetheless, we can
99 still measure the distance from the pre-pandemic attractor and ask how the distance
100 changes over time (Figure 2E). The LOESS fit suggests that the distance from the
101 pre-pandemic attractor will initially decrease exponentially on average (equivalently,
102 linearly on a log scale) and eventually plateau (Figure 2F). Here, a permanent 10%
103 reduction in transmission rate slows the system, which causes the distance from the
104 pre-pandemic attractor initially to decrease at a slower rate (Figure 2F) than it would
105 have otherwise (Figure 2C) before plateauing at a fixed distance between the two
106 attractors. This example shows that resilience is not necessarily an intrinsic prop-
107 erty of a specific pathogen. Instead, pathogen resilience is a property of a specific
108 attractor that a host-pathogen system approaches, which depends on both pathogen
109 and host characteristics.

110 Finally, transient phenomena can further complicate the picture (Figure 2G–
111 I). For example, a stage-structured model initially exhibits a stable annual cycle,
112 but perturbations from NPIs cause the epidemic to shift to biennial cycles (Figure
113 2G). The system eventually approaches the original pre-pandemic attractor (Figure
114 2H), suggesting that this biennial cycle is a transient phenomenon. The LOESS fit
115 indicates that the distance from the attractor initially decreases exponentially at a
116 rate that is consistent with the intrinsic resilience of the seasonally unforced stage-

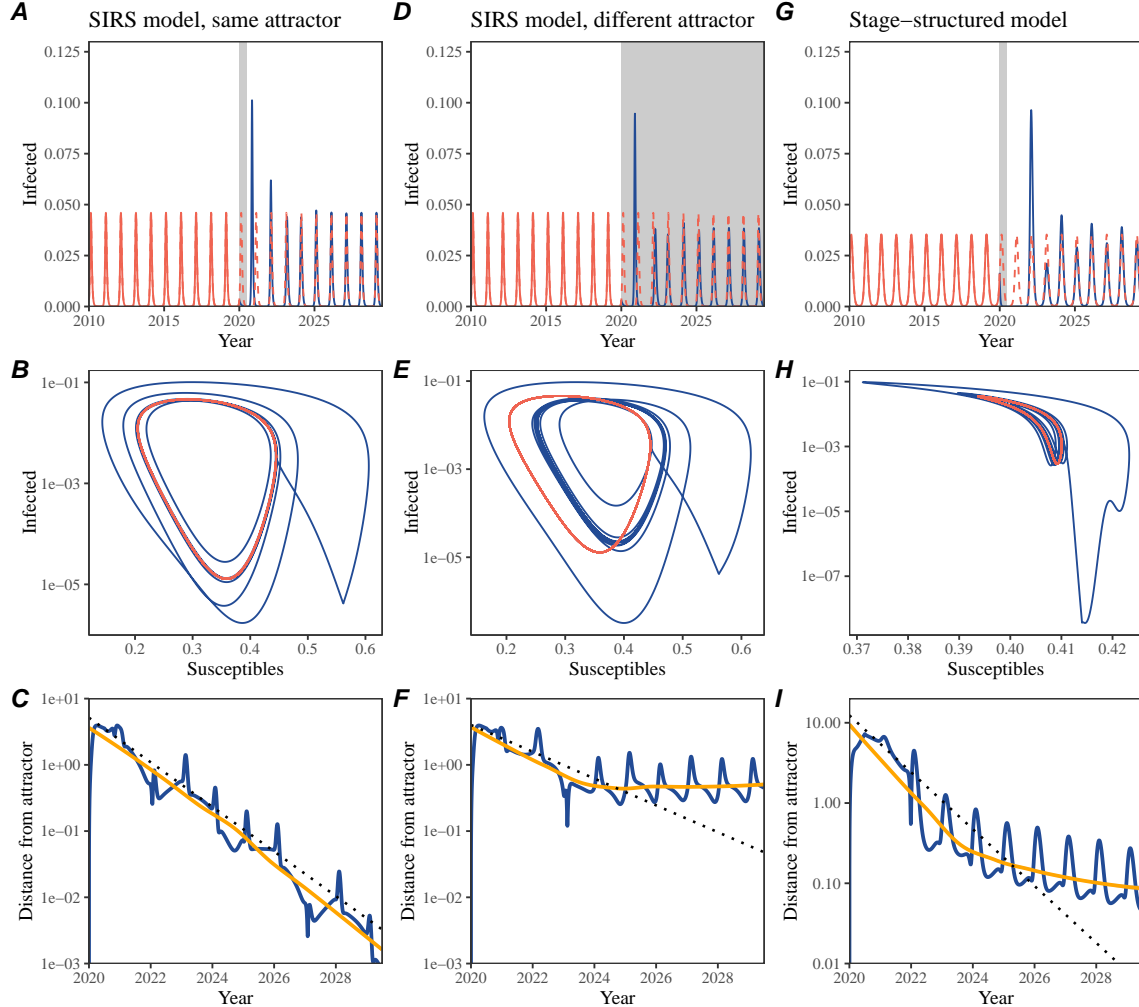


Figure 2: A simple method to measure pathogen resilience following NPIs across different scenarios. (A, D, G) Simulated epidemic trajectories across various models. Red and blue solid lines represent epidemic dynamics before and after interventions are introduced, respectively. Red dashed lines represent counterfactual epidemic dynamics in the absence of interventions. Gray regions indicate the duration of interventions. (B, E, H) Phase plane representation of the epidemic dynamics from corresponding models. Red and blue solid lines represent epidemic trajectories on an SI phase plane before and after interventions are introduced, respectively. (C, F, I) Changes in logged distance from the attractor over time. Blue lines represent the logged distance from the attractor. Orange lines represent the locally estimated scatterplot smoothing (LOESS) fits to the logged distance from attractor. Dotted lines show the intrinsic resilience of the seasonally unforced system.

117 structured system, but the rate of decrease decelerates with the damped oscillations
 118 (Figure 2I). This behavior is also referred to as a ghost attractor, which causes long

119 transient dynamics and slow transitions [16]. Strong seasonal forcing in transmission
120 can also lead to transient phenomena for a simple SIRS model, causing a slow return
121 to pre-perturbation dynamics (Supplementary Figure S1).

122 We also explore measuring the resilience of a two-strain host-pathogen system:
123 when the dynamics two strains (or two pathogens) are coupled through cross immu-
124 nity, we would expect the entire system to be characterized by a single resilience value
125 (rather than having two separate resilience for each strain). Simulations from a sim-
126 ple two-strain system illustrate that separate analyses of individual strain dynamics
127 (e.g., RSV A vs B) and a joint analysis of total infections (e.g., total RSV infections)
128 (Supplementary Figure S2, 3). *[SWP: This is expected because the phase portaits
129 of each of the coupled strains are projections of the shared attractor, according to
130 Takens Theorem. (Is this precisely correct?)]* Analogous to a single system, strong
131 seasonal forcing in transmission can cause the system to slow down through transient
132 phenomena (Supplementary Figure S4).

133 These observations indicate three possibilities. First, we can directly estimate
134 the empirical resilience of a host-pathogen system by looking at how fast the system
135 approaches a pre-pandemic attractor, provided that we can measure the distance
136 from attractor. The empirical approach to estimating pathogen resilience is partic-
137 ularly convenient because it does not require us to know the true underlying model;
138 estimating the intrinsic resilience from fitting misspecified models can lead to bi-
139 ased estimates (Supplementary Figure S5). Second, resilience estimates allow us to
140 make phenomenological predictions about the dynamics of a host-pathogen system
141 following a perturbation: assuming that the distance from the attractor will decrease
142 exponentially over time, we can obtain a ballpark estimate for when the system will
143 reach an attractor. Finally, deviation from an exponential decrease in the distance
144 from attractor can provide information about whether the system has reached an
145 alternative attractor, or a ghost attractor, that is different from the original, pre-
146 pandemic attractor. These alternative attractors may reflect continued perturbations
147 from permanent changes in transmission patterns as well as changes in immune land-
148 scapes.

149 Inferring pathogen resilience from real data

150 Based on these observations, we now lay out our approach to estimating pathogen
151 resilience from real data (Figure 3). We then test this approach against simulations
152 and apply it to real data.

153 So far, we focused on simple examples that assume a constant transmission re-
154 duction. However, in practice, the impact of NPIs on pathogen transmission is
155 likely more complex (Figure 3A), reflecting introduction and relaxation of various
156 intervention strategies. These complexities can lead to longer delays between the
157 introduction of NPIs and pathogen re-emergence as well as temporal variation in
158 outbreak sizes (Figure 3B): in this example, continued transmission reduction from

159 NPIs limits the size of the first outbreak in 2021 following the emergence, allowing
160 for a larger outbreak in 2022 when NPIs are further relaxed.

161 Previously, we relied on the dynamics of susceptible and infected hosts to com-
162 pute the distance from attractor (Figure 2), but information on susceptible hosts is
163 rarely available in practice. In addition, uncertainties in case counts due to observa-
164 tion error as well as the possibility of complex, multiannual attractor add challenges
165 to measuring the distance from attractor. To address these challenges, we first re-
166 construct an empirical attractor by utilizing Takens’ theorem, which states that an
167 attractor of a nonlinear multidimensional system can be mapped onto a delayed em-
168 bedding [14]. Here, we use delayed copies of logged values of pre-pandemic cases
169 $C(t)$ (Figure 3C) to reconstruct the attractor:

$$\langle \log(C(t) + 1), \log(C(t - \tau) + 1), \dots, \log(C(t - (M - 1)\tau) + 1) \rangle, \quad (1)$$

170 where the delay τ and embedding dimension M are determined based on autocor-
171 relations and false nearest neighbors, respectively [17, 18]. We then apply the same
172 delay and embedding dimensions to the entire time series to determine the position
173 on a multi-dimensional state space (Figure 3D), which allows us to measure the
174 nearest neighbor distance between the current state of the system and the empirical
175 pre-pandemic attractor (Figure 3E). In principle, we can quantify how fast this dis-
176 tance decreases by fitting a linear regression on a log scale, where the slope of the
177 linear regression corresponds to pathogen resilience. Overall temporal variations in
178 the distance from attractor, especially the observed rate of decrease, appear robust
179 to choices about embedding delays and dimensions; using longer delays and higher
180 dimensions tends to smooth out temporal variations in the distance from attractor
181 (Supplementary Figure S6).

182 Complex changes in the distance from attractor suggest that estimating pathogen
183 resilience from linear regression will likely be sensitive to our choice of fitting win-
184 dows for the regression (Figure 3E). In Supplementary Materials, we explore an
185 automated window selection criterion for linear regression and test it against ran-
186 domized, stochastic simulations across a wide range of realistic NPI shapes. We find
187 that resilience estimates based on the automated window selection criterion are mod-
188 erately correlated ($\rho = 0.48$) with the intrinsic resilience of the post-NPI attractor
189 (Supplementary Figure S7). In contrast, a naive approach that uses the entire time
190 series, starting from the peak distance, only gives a correlation coefficient of $\rho = 0.09$
191 and consistently underestimates the intrinsic resilience (Supplementary Figure S7).

192 Now, we apply this approach to pathogen surveillance data presented in Figure
193 1. For each time series, we apply Takens’ theorem independently to reconstruct
194 the empirical attractor and obtain the corresponding time series of distances from
195 attractors (Supplementary Figure S8 for the distance time series and linear regression
196 fits). Then, we use the automated window selection criterion to fit a linear regression
197 and estimate the empirical resilience for each pathogen in each country. For most
198 respiratory pathogens, resilience estimates fall between 0.4/year and 1.8/year (Figure
199 4A), with the exception of rhinovirus in the US (0.066/year; 95% CI: 0.018/year–

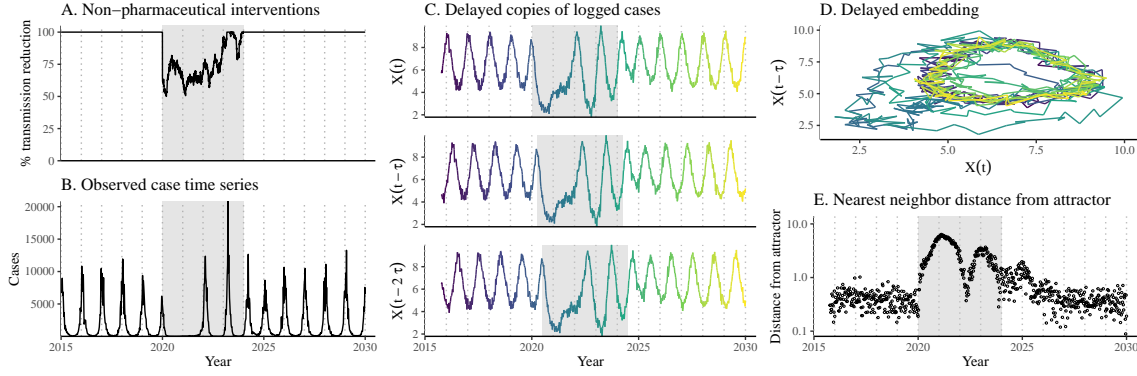


Figure 3: A schematic diagram explaining the inference of pathogen resilience from synthetic data. (A) A realistic example of a synthetic NPI, represented by a relative reduction in transmission. (B) The impact of the synthetic NPI on epidemic dynamics simulated using a SIRS model with demographic stochasticity. (C) Generating delayed copies of the logged time series allows us to obtain an embedding. (D) Two dimensional representation of an embedding. (E) Delayed embedding allows us to calculate the nearest neighbor distance from the empirical attractor, which is determined based on the pre-pandemic time series. This distance time series can be used to infer pathogen resilience after choosing an appropriate window for linear regression.

0.113/year) and bocavirus in Korea (0.087/year; 95% CI: 0.023/year–0.151/year). Excluding these exceptions, the mean resilience of common respiratory pathogens is 0.974/year (95% CI: 0.784/year–1.16/year). As a reference, this is ≈ 7 times higher than the intrinsic resilience of pre-vaccination measles in England and Wales ($\approx 0.13/\text{year}$). Finally, resilience estimates for norovirus appears to be comparable to the intrinsic resilience of measles: 0.119/year (95%CI: 0.004/year–0.233/year) for Korea and 0.385/year (95% CI: 0.167/year–0.603/year). A simple ANOVA shows that there are significant differences in resilience estimates across countries ($p < 0.036$) and pathogens ($p < 0.030$).

Using resilience estimates, we now predict when each pathogen will return to their original pre-pandemic cycles. Specifically, we extend our linear regression fits to distance-from-attractor time series and ask when the predicted regression line will cross a threshold value, which we set equal to the mean of pre-pandemic distances. We predict that a return to pre-pandemic cycles would be imminent for most pathogens (Figure 4B; see Supplementary Figure S9 for a zoomed out version). We also predict that many pathogens should have already returned to their pre-pandemic dynamics by the end of 2024, but these predictions contradict some of the observed pathogen dynamics. For example, we predict that both human metapneumovirus and RSV in Korea should have returned to their attractors by now, but the magnitude and timing of recent epidemics are different from pre-pandemic patterns (Figure 1). These observations suggest the possibility that some common respiratory pathogens

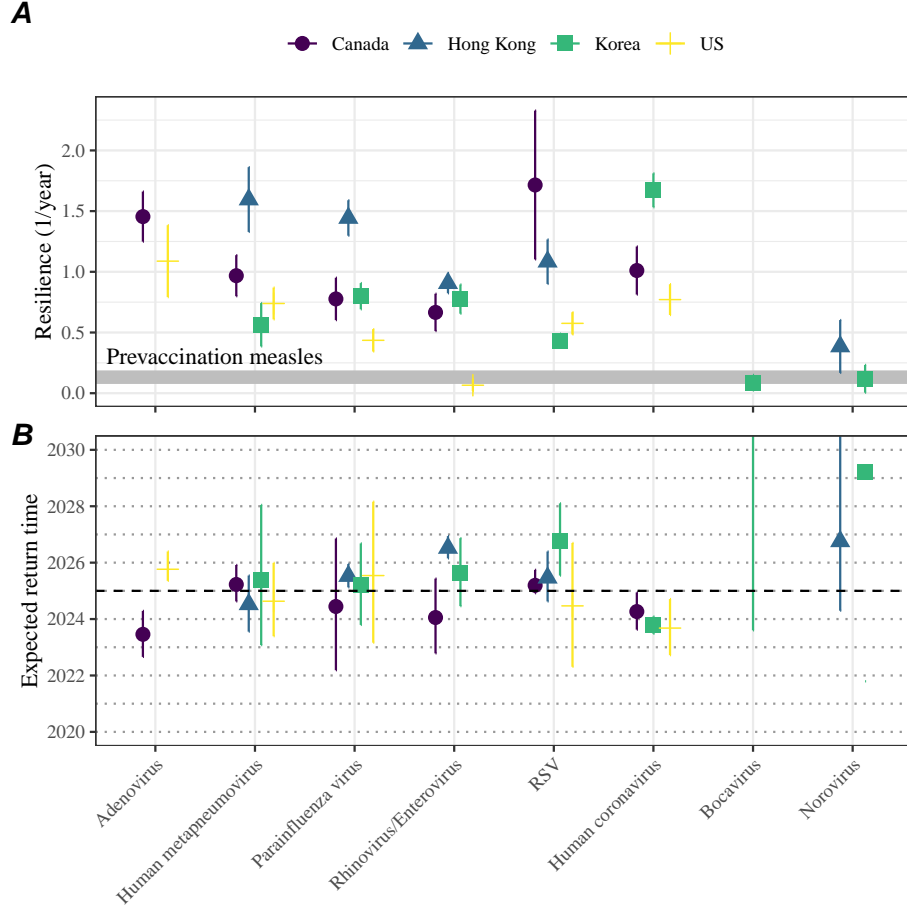


Figure 4: **Summary of resilience estimates.** (A) Estimated pathogen resilience. The gray horizontal line represents the intrinsic resilience of pre-vaccination measles dynamics. (B) Predicted timing of when each pathogen will return to their pre-pandemic cycles. The dashed line in panel B indicates the end of 2024 (current observation time). Error bars represent 95% confidence intervals.

221 may have converged to different attractors.

222 In Supplementary Materials, we also consider using a lower threshold for the false
 223 nearest neighbor approach when determining the embedding dimension; this gives a
 224 higher embedding dimension. As explained earlier (Supplementary Figure S6), this
 225 gives a smoother distance-from-attractor time series (compare Supplementary Figure
 226 S10 with S8); this also requires us to use longer time series, which prevents us from
 227 estimating resilience for some pathogens. Overall, resulting estimates of pathogen
 228 resilience with higher embedding dimensions still mostly fall between 0.3/year and
 229 2.1/year (Supplementary Figure S11). A direct comparison between two approaches
 230 (i.e., original estimate vs using higher dimensions) shows a strong consistency in
 231 resilience estimates (Supplementary Figure S12).

232 **Susceptible host dynamics explain variation in pathogen
233 resilience**

234 So far, we focused on quantifying pathogen resilience from the observed patterns
235 of pathogen re-emergence following COVID-19 interventions. But what factors de-
236 termine how resilient a host-pathogen system is? Here, we use the SIRS model to
237 show that susceptible host dynamics are the key determinants of pathogen resilience.
238 To do so, we vary the basic reproduction number \mathcal{R}_0 , which represents the average
239 number of secondary infections caused by a newly infected individual in a fully sus-
240 ceptible population, and the duration of immunity and compute intrinsic resilience
241 for each parameter.

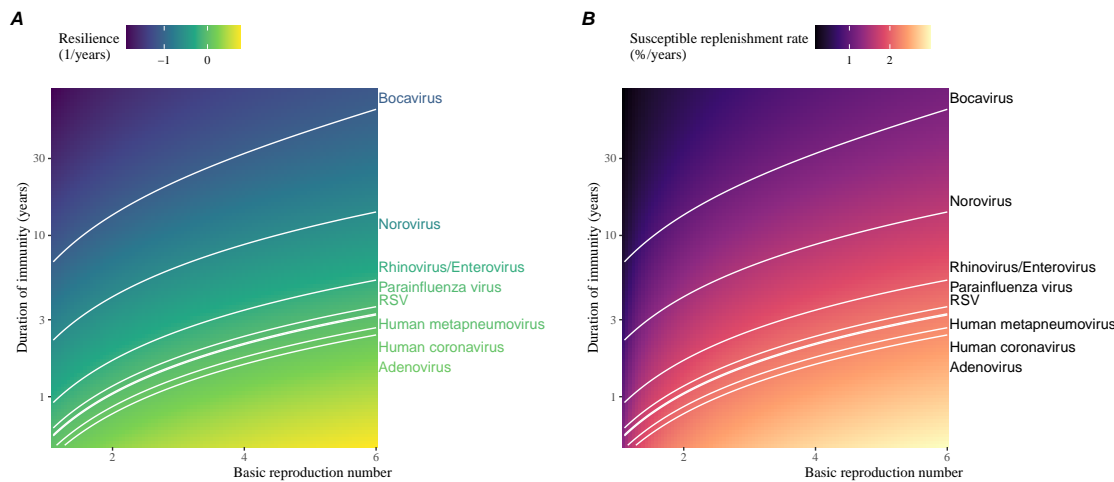


Figure 5: **Linking pathogen resilience to epidemiological parameters and susceptible host dynamics.** (A) The heat map represents intrinsic resilience as a function of the basic reproduction number \mathcal{R}_0 and the duration of immunity. (B) The heat map represents per-capita susceptible replenishment rate as a function of the basic reproduction number \mathcal{R}_0 and the duration of immunity. The standard SIRS model is used to compute intrinsic resilience and per-capita susceptible replenishment rate. Lines correspond to a set of parameters that are consistent with mean resilience estimates for each pathogen. Pathogens are ranked based on their mean resilience estimates, averaged across different countries.

242 We find an increase in \mathcal{R}_0 and a decrease in duration of immunity correspond
243 to an increase in pathogen resilience (Figure 5A). These variations can be under-
244 stood in terms of the susceptible host dynamics, where faster per-capita susceptible
245 replenishment rate causes the system to be more resilient (Figure 5B). This rate can
246 be expressed as a ratio between absolute rate at which new susceptibles enter the
247 population and the equilibrium number of susceptible individuals in the population,
248 \bar{S} . Therefore, both higher \mathcal{R}_0 and shorter duration of immunity can drive faster

249 per-capita susceptible replenishment rate (Figure 5B), especially because higher \mathcal{R}_0
250 leads to lower \bar{S} .

251 Finally, we can rank different pathogens based on the average values of empirical
252 resilience computed previously, which allows us to determine a set of parameters that
253 are consistent with the estimated resilience (Figure 5A). Across all pathogens we
254 consider, except for bocavirus and norovirus, we estimate that the average duration
255 of immunity is likely to be short (< 6 years) across a plausible range of \mathcal{R}_0 . These
256 rankings further allow us to map each pathogen onto a set of SIRS parameters that
257 are consistent with its empirical resilience (Figure 5A) and obtain a plausible range
258 of susceptible replenishment rates for each pathogen (Figure 5B). However, we note
259 that there is no one-to-one correspondence between susceptible replenishment rates
260 and pathogen resilience, leading to a wide uncertainty in the estimates for susceptible
261 replenishment rates (Figure 5B).

262 Discussion

263 The COVID-19 interventions have caused major disruptions to circulation patterns of
264 both respiratory and non-respiratory pathogens, adding challenges to predicting their
265 future dynamics [1, 2, 3, 4]. However, these interventions offer large-scale natural
266 experiments for understanding how different pathogens respond to perturbations. In
267 this study, we show that pathogen re-emergence patterns following COVID-19 inter-
268 ventions can be characterized through the lens of ecological resilience. Traditionally,
269 ecological resilience measures how fast a system returns to a reference state following
270 a perturbation. In the context of respiratory pathogens, resilience measures how fast
271 epidemics return to their endemic cycles after interventions are lifted.

272 We use an attractor reconstruction approach to quantify how distance from at-
273 tractor changes over time for each pathogen [14]. We show that the resilience of
274 a host-pathogen system can be estimated by fitting a linear regression to a logged
275 distance-from-attractor time series. Overall, we estimate that the resilience for most
276 common respiratory pathogens ranges between 0.4/year and 1.8/year, which is 3–14
277 times more resilient than prevaccination measles, indicating potential challenges in
278 controlling common respiratory pathogens.

279 Our framework allows us to make phenomenological predictions about when each
280 pathogen will return to their endemic cycles. The ability to predict future epidemic
281 patterns from resilience estimates offers a new paradigm for epidemic forecasting.
282 While this approach cannot predict the exact timing of outbreaks or epidemic pat-
283 terns, it is nonetheless useful for predicting when epidemics will settle down to regular
284 cycles after a large perturbation, such as COVID-19 interventions.

285 Our analyses suggest a possibility that several pathogens may have converged
286 to different endemic cycles compared to their pre-pandemic epidemic patterns. Key
287 examples include human metapnuemovirus, RSV, and bocavirus in Korea as well as
288 RSV in Hong Kong. These changes may reflect changes in surveillance or actual shift

in the dynamics, caused by permanent changes in behavior or population-level immunity. While it seems unlikely that permanent changes in behavior would only affect a few pathogens and not others, we cannot rule out this possibility given heterogeneity in the age of infection across different respiratory pathogens [SWP: CITE]. A shift in population-level immunity is plausible, as the emergence of SARS-CoV-2 and extinction of influenza B/Yamagata likely caused major changes in immune landscapes; interactions among co-circulating pathogens, such as cross immunity between RSV and HMPV [19], may have also contributed to changes in population-level immunity. However, we currently do not know how immunity, or lack thereof, from these pathogens would affect infection from other pathogens. Future studies should use detailed mechanistic models, coupled with behavioral and immunological data, to test these hypotheses and better understand post-pandemic dynamics of endemic pathogens.

We show that susceptible host dynamics shape pathogen resilience, where faster replenishment of the susceptible population causes the pathogen to be more resilient. For simplicity, we focus on waning immunity and birth as the main drivers of the susceptible host dynamics but other mechanisms can also contribute to the replenishment of the susceptible population. In particular, pathogen evolution, especially the emergence of antigenically novel strains, can cause effective waning of immunity in the population; therefore, we hypothesize that faster rates of antigenic evolution can also cause a pathogen to be more resilient. Future studies should explore the relationship between the rate of evolution and resilience for antigenically evolving pathogens.

Quantifying pathogen resilience also offers novel approaches to validating population-level epidemiological models. So far, most of model validation in infectious disease ecology is based on the ability of a model to reproduce the observed epidemic dynamics and to predict future dynamics [20, 19, 21, 22, 23]. However, many models can perform similarly under these criteria. For example, two major RSV models have been proposed to explain biennial epidemic patterns: (1) a stage- and age-structured model that allows disease severity to vary with number of past infections and age of infection [21] and (2) a pathogen-interaction model that accounts for cross immunity between RSV and human metapneumovirus [19]. Since both models can accurately reproduce the observed epidemic patterns, standard criteria for model validation do not allow us to distinguish between these two models from population-level data alone. Instead, we can measure the empirical resilience of each model by simulating various perturbations and compare them to estimates of empirical resilience from data, using COVID-19 interventions as an opportunity.

There are several limitations to our work. First, we did not extensively explore other approaches to reconstructing the attractor. Recent studies showed that more sophisticated approaches, such as using non-uniform embedding, can provide more robust reconstruction for noisy data [18]. In the context of causal inference, choices about embedding can have major impact on the resulting inference [24]. Our resilience estimates are likely overly confident given a lack of uncertainties in attractor

332 reconstruction as well as the simplicity of our statistical framework. Short pre-
333 pandemic time series also contribute to the crudeness of our estimates. Nonetheless,
334 as illustrated in our sensitivity analyses (Supplementary Figure S6, S10–S12), inferences
335 about pathogen resilience in our SIRS model appear to be robust to decisions
336 about embedding lags and dimensions—this is because tracking the rate at which
337 the system approaches the attractor is likely a much simpler problem than making
338 inferences about causal directionality. Our qualitative prediction that common res-
339piratory pathogens are more resilient than prevaccination measles is also likely to be
340 robust to these predictions, given how rapid many respiratory pathogens returned to
341 their original cycles following COVID-19 interventions.

342 Predicting the impact of anthropogenic changes on infectious disease dynam-
343 ics is a fundamental aim of infectious disease research in a rapidly changing world.
344 Our study illustrates that quantifying pathogen resilience can help us understand
345 how infectious disease pathogens respond to major perturbations caused by public
346 health interventions. More broadly, a detailed understanding of the determinants of
347 pathogen resilience may offer unique insights into pathogen persistence and control-
348 lability.

349 Materials and Methods

350 Data

351 We gathered time series on respiratory infections from Canada, Hong Kong, Korea,
352 and United States (US). As a reference, we also included time series data on norovirus
353 infections for available countries—in contrast to respiratory pathogens, we expect
354 gastrointestinal viruses, such as norovirus, to be differently affected by COVID-19
355 intervention measures. For all time series, we rounded every year to 52 weeks by
356 taking the average number of cases and tests between the 52nd and 53rd week. We
357 also rescale all time series to account for changes in testing patterns, which are then
358 used for the actual analysis.

359 Weekly time series of respiratory infection cases in Canada comes from the Res-
360piratory Virus Detection Surveillance System, which collect data from select labo-
361ratories across Canada. We extracted the data from <https://www.canada.ca/en/public-health/services/surveillance/respiratory-virus-detections-canada.html>.
362 To account for an increase in testing from 2013 to 2024, we calculate a 2 year
363 moving average for the number of tests for each pathogen, which we use as a proxy
364 for testing effort. Then, we divide the smoothed testing patterns by the smoothed
365 value at the final week such that the testing effort has a maximum of 1. We then
366 divide weekly cases by the testing effort to obtain a scaled case time series. A similar
367 approach was used earlier for the analysis of RSV time series in the US [21].

368 Weekly time series of respiratory infection cases in Hong Kong comes from the
369 Centre for Health Protection, Department of Health. We extract the data from
370 <https://www.chp.gov.hk/en/statistics/data/10/641/642/2274.html>. We also

372 apply the same scaling procedure to the time series as we did for Canada. For Hong
373 Kong, we only adjust for testing efforts up to the end of 2019 because there was a
374 major reduction in testing for common respiratory pathogens since 2020.

375 Weekly time series of acute respiratory infection cases in Korea comes from Ko-
376 rea Disease Control and Prevention Agency. We extract the data from <https://dportal.kdca.go.kr/pot/is/st/ari.do>. While we do not have information on
377 testing, the reported number of respiratory infections consistently increased from
378 2013 to the end of 2019, which we interpreted as changes in testing patterns. Since
379 we do not have testing numbers, we used the weekly sum of all acute respiratory vi-
380 ral infection cases as a proxy for testing, which were further smoothed with moving
381 averaged and scaled to have a maximum of 1. For Korea, we also only adjust for
382 testing efforts up to the end of 2019.

383 Finally, weekly time series of respiratory infection cases in the US comes from
384 the National Respiratory and Enteric Virus Surveillance System. In the US, there
385 has been a large increase in testing against some respiratory pathogens, especially
386 RSV, which could not be corrected for through simple scaling. Instead, we derive an
387 incidence proxy by multiplying the test positivity with influenza-like illness positivity,
388 which is taken from <https://gis.cdc.gov/grasp/fluview/fluportaldashboard.html>. This method of estimating an incidence proxy has been recently applied in
389 the analysis of seasonal coronaviruses [7] and Mycoplasma pneumoniae infections [4].
390 Detailed assumptions and justifications are provided in [25].

393 Estimating pathogen resilience

394 In order to measure pathogen resilience from surveillance data, we first reconstruct
395 the empirical pre-pandemic attractor of the system using Takens' embedding theorem
396 [14]. Specifically, for a given pathogen, we take the pre-pandemic (before 2020)
397 case time series $C(t)$ and reconstruct the attractor using delayed embedding with a
398 uniform delay of τ and dimension M :

$$X_{\tau,m}(t) = \langle \log(C(t) + 1), \log(C(t - \tau) + 1), \dots, \log(C(t - (M - 1)\tau) + 1) \rangle. \quad (2)$$

399 Here, the delay τ is determined by calculating the autocorrelation of the logged pre-
400 pandemic time series and asking when the autocorrelation crosses 0 for the first time
401 [18]; a typical delay for an annual outbreak is around 13 weeks.

402 Then, for a given delay τ , we determine the embedding dimension M using the
403 false nearest neighbors approach [17, 18]. To do so, we start with an embedding
404 dimension e and construct a set of points $A_{\tau,e} = \{X_{\tau,e}(t) | t < 2020\}$. Then, for
405 each point $X_{\tau,e}(t)$, we determine the nearest neighbor from the set $A_{\tau,e}$, which we
406 denote $X_{\tau,e}(t_{nn})$ for $t \neq t_{nn}$. Then, if the distance between these two points on $e + 1$
407 dimension, $D_{\tau,e+1}(t) = \|X_{\tau,e+1}(t_{nn}) - X_{\tau,e+1}(t)\|_2$, is larger than their distance on
408 e dimension, $D_{\tau,e}(t) = \|X_{\tau,e}(t_{nn}) - X_{\tau,e}(t)\|_2$, these two points are deemed to be
409 false nearest neighbors; specifically, we use a threshold R for the ratio between two
410 distances $D_{\tau,e+1}(t)/D_{\tau,e}(t)$ to determine false nearest neighbors. In the main text, we

411 determine the embedding dimension based on the first dimension without any false
 412 nearest neighbors for $R = 10$. In Supplementary Materials, we impose $R = 5$ to select
 413 for higher dimensions. Once we determine the embedding lag τ and dimension M ,
 414 we apply the embedding to the entire time series and calculate the nearest neighbor
 415 distance against the attractor $A_{\tau,M}$ to obtain a time series of distance from attractor
 416 $D_{\tau,M}(t)$.

417 From a time series of distances from the attractor, we estimate pathogen resilience
 418 by fitting a linear regression to an appropriate window. To automatically select
 419 the fitting window, we begin by smoothing the distance time series using locally
 420 estimated scatterplot smoothing (LOESS) to obtain $\hat{D}_{\tau,M}(t)$, where the smoothing
 421 is performed on a log scale and exponentiated afterwards. Then, we determine
 422 threshold values (T_{start} and T_{end}) for the smoothed distances and choose the fitting
 423 window based on when $\hat{D}_{\tau,M}(t)$ crosses these threshold values for the first time.
 424 These thresholds are determined by first calculating maximum distance,

$$\max \hat{D} = \max \hat{D}_{\tau,M}(t), \quad (3)$$

425 and mean pre-pandemic distance,

$$\hat{D}_{\text{mean}} = \frac{1}{N_{t < 2020}} \sum_{t < 2020} \hat{D}_{\tau,M}(t), \quad (4)$$

426 as a reference, and then dividing their ratios into 10 equal bins:

$$T_{\text{start}} = \hat{D}_{\text{mean}} \times \left(\frac{\max \hat{D}}{\hat{D}_{\text{mean}}} \right)^{9/10} \quad (5)$$

$$T_{\text{end}} = \hat{D}_{\text{mean}} \times \left(\frac{\max \hat{D}}{\hat{D}_{\text{mean}}} \right)^{1/10} \quad (6)$$

427 This allows us to discard the initial period during which the distance increases (from
 428 the introduction of intervention measures) and the final period during which the
 429 distance plateaus (as the system reaches an attractor). The fitting window is deter-
 430 mined based on when the smoothed distance $\hat{D}_{\tau,M}(t)$ crosses these threshold values
 431 for the first time; then, we fit a linear regression to logged (unsmoothed) distances
 432 $\log D_{\tau,M}(t)$ using that window.

433 Mathematical modeling

434 Throughout the paper, we use a series of mathematical models to illustrate the con-
 435 cept of pathogen resilience and to understand the determinants of pathogen resilience.
 436 In general, the intrinsic resilience for a given system is given by the largest real part
 437 of the eigenvalues of the linearized system at endemic equilibrium. Here, we focus on
 438 the SIRS model and present the details of other models in Supplementary Materials.

439 The SIRS (Susceptible-Infected-Recovered-Susceptible) model is the simplest model
 440 that allows for waning of immunity, where recovered (immune) individuals are as-
 441 sumed to become fully susceptible after an average of $1/\delta$ time period. The dynamics
 442 of the SIRS model is described by the following set of differential equations:

$$\frac{dS}{dt} = \mu - \beta(t)SI - \mu S + \delta R \quad (7)$$

$$\frac{dI}{dt} = \beta(t)SI - (\gamma + \mu)I \quad (8)$$

$$\frac{dR}{dt} = \gamma I - (\delta + \mu)R \quad (9)$$

(10)

443 where μ represents the birth/death rate, $\beta(t)$ represents the time-varying trans-
 444 mission rate, and γ represents the recovery rate. The basic reproduction number
 445 $\mathcal{R}_0(t) = \beta(t)/(\gamma + \mu)$ is defined as the average number of secondary infections caused
 446 by a single infected individual in a fully susceptible population and measures the
 447 intrinsic transmissibility of a pathogen.

448 When we first introduce the idea of pathogen resilience (Figure 2), we impose
 449 sinusoidal changes to the transmission rate to account for seasonal transmission:

$$\beta(t) = b_1(1 + \theta \cos(2\pi(t - \phi)))\alpha(t), \quad (11)$$

450 where b_1 represents the baseline transmission rate, θ represents the seasonal ampli-
 451 tude, and ϕ represents the seasonal offset term. Here, we also introduce an extra
 452 multiplicative term $\alpha(t)$ to account for the impact of COVID-19 interventions, where
 453 $\alpha(t) < 1$ indicates transmission reduction. Figure 2A and 2B are generated assuming
 454 $b_1 = 3 \times (365/7 + 1/50)/\text{years}$, $\theta = 0.2$, $\phi = 0$, $\mu = 1/50/\text{years}$, $\gamma = 365/7/\text{years}$, and
 455 $\delta = 1/2/\text{years}$. In Figure 2A, we impose a 50% transmission reduction for 6 months
 456 from 2020:

$$\alpha(t) = \begin{cases} 0.5 & 2020 \leq t < 2020.5 \\ 1 & \text{otherwise} \end{cases} \quad (12)$$

457 In Figure 2B, we impose a 50% transmission reduction for 6 months from 2020 and
 458 a permanent 10% reduction onward:

$$\alpha(t) = \begin{cases} 1 & t < 2020 \\ 0.5 & 2020 \leq t < 2020.5 \\ 0.9 & 2020.5 \leq t \end{cases} \quad (13)$$

459 In both scenarios, we simulate the SIRS model from the following initial conditions
 460 ($S(0) = 1/\mathcal{R}_0$, $I(0) = 1 \times 10^{-6}$, and $R(0) = 1 - S(0) - I(0)$) from 1900 until 2030.

461 To measure the empirical resilience of the SIR model (Figure 2C and 2F), we
 462 compute the normalized distance between post-intervention susceptible and logged

⁴⁶³ infected proportions and their corresponding pre-intervention values at the same time
⁴⁶⁴ of year:

$$\sqrt{\left(\frac{S(t) - S_{\text{pre}}(t)}{\sigma_S}\right)^2 + \left(\frac{\log I(t) - \log I_{\text{pre}}(t)}{\sigma_{\log I}}\right)^2}, \quad (14)$$

⁴⁶⁵ where σ_S and $\sigma_{\log I}$ represent the standard deviation in the pre-intervention suscep-
⁴⁶⁶ tible and logged infected proportions. We normalize the differences in susceptible
⁴⁶⁷ and logged infected proportions to allow both quantities to equally contribute to the
⁴⁶⁸ changes in distance from attractor. In Supplementary Materials, we also compare
⁴⁶⁹ the how the degree of seasonal transmission affects empirical resilience by varying
⁴⁷⁰ θ from 0 to 0.4; when we assume no seasonality ($\theta = 0$), we do not normalize the
⁴⁷¹ distance because the standard deviation of pre-intervention dynamics are zero.

⁴⁷² Finally, we use the SIRS model to understand how underlying epidemiological
⁴⁷³ parameters affect pathogen resilience and link this relationship to underlying sus-
⁴⁷⁴ ceptible host dynamics. For the simple SIRS model without seasonal transmission
⁴⁷⁵ ($\theta = 0$), the intrinsic resilience corresponds to:

$$-\frac{\text{Re}(\lambda)}{2} = \frac{\delta + \beta I^* + \mu}{2}. \quad (15)$$

⁴⁷⁶ Here, I^* represents the prevalence values at endemic equilibrium:

$$I^* = \frac{(\delta + \mu)(\beta - (\gamma + \mu))}{\beta(\delta + \gamma + \mu)}. \quad (16)$$

⁴⁷⁷ The susceptible replenishment rate is given by:

$$S_{\text{replenish}} = \frac{\mu + \delta R}{S^*}, \quad (17)$$

⁴⁷⁸ where $S^* = 1/\mathcal{R}_0$ represents the equilibrium proportion of susceptible individuals.
⁴⁷⁹ We vary the basic reproduction number \mathcal{R}_0 between 1.1 to 6 and the average duration
⁴⁸⁰ of immunity $1/\delta$ between 2 to 80 years, and compute these two quantities. In doing
⁴⁸¹ so, we fix all other parameters: $\mu = 1/80/\text{years}$ and $\gamma = 365/7/\text{years}$.

482 **Supplementary Text**

483 **Resilience of a stage-structured system.**

484 In Figure 2G–I, we use a more realistic, stage-structured model to illustrate how
 485 transient phenomena can cause the system to slow down. Specifically, we use the
 486 stage-structured RSV model proposed by [21], which assumes that subsequent rein-
 487 fections cause an individual to become less susceptible and transmissible than previ-
 488 ous infections. The model dynamics can be described as follows:

$$\frac{dM}{dt} = \mu - (\omega + \mu)M \quad (S1)$$

$$\frac{dS_0}{dt} = \omega M - (\lambda(t) + \mu)S_0 \quad (S2)$$

$$\frac{dI_1}{dt} = \lambda(t)S_0 - (\gamma_1 + \mu)I_1 \quad (S3)$$

$$\frac{dS_1}{dt} = \gamma_1 I_1 - (\sigma_1 \lambda(t) + \mu)S_1 \quad (S4)$$

$$\frac{dI_2}{dt} = \sigma_1 \lambda(t)S_1 - (\gamma_2 + \mu)I_2 \quad (S5)$$

$$\frac{dS_2}{dt} = \gamma_2 I_2 - (\sigma_2 \lambda(t) + \mu)S_2 \quad (S6)$$

$$\frac{dI_3}{dt} = \sigma_2 \lambda(t)S_2 - (\gamma_3 + \mu)I_3 \quad (S7)$$

$$\frac{dS_3}{dt} = \gamma_3 I_3 - (\sigma_3 \lambda(t) + \mu)S_3 + \gamma_4 I_4 \quad (S8)$$

$$\frac{dI_4}{dt} = \sigma_3 \lambda(t)S_3 - (\gamma_4 + \mu)I_4 \quad (S9)$$

(S10)

489 where M represents the proportion of individuals who are maternally immune; S_i
 490 represents the proportion of individuals who are susceptible after i prior infections; I_i
 491 represents the proportion of individuals who are currently (re)-infected with their i -th
 492 infection; μ represents the birth and death rates; $1/\omega$ represents the mean duration
 493 of maternal immunity; $1/\gamma_i$ represents the mean duration of infection; $\lambda(t)$ represents
 494 the force of infection; and σ_i represents the reduction in susceptibility for reinfection.
 495 The force of infection is modeled using a sinusoidal function:

$$\beta(t) = b_1(1 + \theta \cos(2\pi(t - \phi)))\alpha(t) \quad (S11)$$

$$\lambda(t) = \beta(I_1 + \rho_1 I_2 + \rho_2(I_3 + I_4)), \quad (S12)$$

496 where b_1 represents the baseline transmission rate; θ represents the seasonal ampli-
 497 tude; ϕ represents the seasonal offset term; $\alpha(t)$ represents the intervention effect;
 498 and ρ_i represents the impact of immunity on transmission reduction. We use the

499 following parameters to simulate the impact of interventions on epidemic dynam-
500 ics [21]: $b_1 = 9 \times (365/10 + 1/80)/\text{years}$, $\theta = 0.2$, $\phi = -0.1$, $\omega = 365/112/\text{years}$,
501 $\gamma_1 = 365/10/\text{years}$, $\gamma_2 = 365/7/\text{years}$, $\gamma_3 = 365/5/\text{years}$, $\sigma_1 = 0.76$, $\sigma_2 = 0.6$,
502 $\sigma_3 = 0.4$, $\rho_1 = 0.75$, $\rho_2 = 0.51$, and $\mu = 1/80/\text{years}$. We assume a 50% transmission
503 reduction for 6 months from 2020:

$$\alpha(t) = \begin{cases} 0.5 & 2020 \leq t < 2020.5 \\ 1 & \text{otherwise} \end{cases} \quad (\text{S13})$$

504 The model is simulated from 1900 to 2030 using the following initial conditions:
505 $M = 0$, $S_0 = 1/\mathcal{R}_0 - I_1$, $I_1 = 1 \times 10^{-6}$, $S_1 = 1 - 1/\mathcal{R}_0$, $I_2 = 0$, $S_2 = 0$, $I_3 = 0$,
506 $S_3 = 0$, and $I_4 = 0$. For the phase plane analysis (Figure 2H) and distance analysis
507 (Figure 2I), we rely on the average susceptibility,

$$\bar{S} = S_0 + \sigma_1 S_1 + \sigma_2 S_2 + \sigma_3 S_3, \quad (\text{S14})$$

508 and total prevalence,

$$I_{\text{total}} = I_1 + I_2 + I_3 + I_4. \quad (\text{S15})$$

509 These quantities are used to compute the normalized distance from the attractor, as
510 described in the main text.

511 Resilience of a multistrain system.

512 We use a simple two-strain model to show that a multistrain host-pathogen system
513 that is coupled through cross immunity can be described by a single resilience value.
514 The model dynamics can be described as follows [19]:

$$\frac{dS}{dt} = \mu - \mu S - (\lambda_1 + \lambda_2)S + \rho_1 R_1 + \rho_2 R_2 \quad (\text{S16})$$

$$\frac{dI_1}{dt} = \lambda_1 S - (\gamma_1 + \mu)I_1 \quad (\text{S17})$$

$$\frac{dI_2}{dt} = \lambda_2 S - (\gamma_2 + \mu)I_2 \quad (\text{S18})$$

$$\frac{dR_1}{dt} = \gamma_1 I_1 - \lambda_2 \epsilon_{21} R_1 - \rho_1 R_1 + \rho_2 R - \mu R_1 \quad (\text{S19})$$

$$\frac{dR_2}{dt} = \gamma_2 I_2 - \lambda_1 \epsilon_{12} R_2 - \rho_2 R_2 + \rho_1 R - \mu R_2 \quad (\text{S20})$$

$$\frac{dJ_1}{dt} = \lambda_1 \epsilon_{12} R_2 - (\gamma_1 + \mu) J_1 \quad (\text{S21})$$

$$\frac{dJ_2}{dt} = \lambda_2 \epsilon_{21} R_1 - (\gamma_2 + \mu) J_2 \quad (\text{S22})$$

$$\frac{dR}{dt} = \gamma_1 J_1 + \gamma_2 J_2 - \rho_1 R - \rho_2 R - \mu R \quad (\text{S23})$$

where S represents the proportion of individuals who are fully susceptible to infections by both strains; I_1 represents the proportion of individuals who are infected with strain 1 without prior immunity; I_2 represents the proportion of individuals who are infected with strain 2 without prior immunity; R_1 represents the proportion of individuals who are fully immune against strain 1 and partially susceptible to reinfection by strain 2; R_2 represents the proportion of individuals who are fully immune against strain 2 and partially susceptible to reinfection by strain 1; J_1 represents the proportion of individuals who are infected with strain 1 with prior immunity against strain 2; J_2 represents the proportion of individuals who are infected with strain 2 with prior immunity against strain 1; R represents the proportion of individuals who are immune to infections from both strains; μ represents the birth/death rate; λ_1 and λ_2 represent the force of infection from strains 1 and 2, respectively; ρ_1 and ρ_2 represent the waning immunity rate; γ_1 and γ_2 represent the recovery rate; ϵ_{12} and ϵ_{21} represent the susceptibility to reinfection with strains 2 and 1, respectively, given prior immunity from infection with strains 1 and 2, respectively. The force of infection is modeled as follows:

$$\beta_1 = b_1(1 + \theta_1 \sin(2\pi(t - \phi_1)))\alpha(t) \quad (\text{S24})$$

$$\beta_2 = b_2(1 + \theta_2 \sin(2\pi(t - \phi_2)))\alpha(t) \quad (\text{S25})$$

$$\lambda_1 = \beta_1(I_1 + J_1) \quad (\text{S26})$$

$$\lambda_2 = \beta_2(I_2 + J_2) \quad (\text{S27})$$

In Supplementary Figures S2–S4, we assume the following parameters: $b_1 = 2 \times 52/\text{years}$, $b_2 = 4 \times 52/\text{years}$, $\phi_1 = \phi_2 = 0$, $\epsilon_{12} = 0.9$, $\epsilon_{21} = 0.5$, $\gamma_1 = \gamma_2 = 52/\text{years}$, $\rho_1 = \rho_2 = 1/\text{years}$, and $\mu = 1/70/\text{years}$. For all simulations, we assume a 50% transmission reduction for 6 months from 2020:

$$\alpha(t) = \begin{cases} 0.5 & 2020 \leq t < 2020.5 \\ 1 & \text{otherwise} \end{cases} \quad (\text{S28})$$

The seasonal amplitude θ is varied from 0 to 0.4. All simulations are ran from 1900 to 2030 from the following initial conditions: $S(0) = 1 - 2 \times 10^{-6}$, $I_1(0) = 1 \times 10^{-6}$, $I_2(0) = 1 \times 10^{-6}$, $R_1(0) = 0$, $R_2(0) = 0$, $J_1(0) = 0$, $J_2(0) = 0$, and $R(0) = 0$.

For this, we consider three different scenarios for measuring pathogen resilience: (1) we only have information about strain 1, (2) we only have information about strain 2, and (3) we are unable to distinguish the differences between strains. In the first two scenarios (see panels A–C for strain 1 and panels D–F for strain 2), we consider the dynamics of average susceptibility for each strain and total prevalence:

$$\bar{S}_1 = S + \epsilon_{12}R_2 \quad (\text{S29})$$

$$\hat{I}_1 = I_1 + J_1 \quad (\text{S30})$$

$$\bar{S}_2 = S + \epsilon_{21}R_1 \quad (\text{S31})$$

$$\hat{I}_2 = I_2 + J_2 \quad (\text{S32})$$

⁵⁴³ In the third scenario (panels G–I), we consider the dynamics of total susceptible and
⁵⁴⁴ infected population:

$$\hat{S} = S + R_2 + R_1 \quad (\text{S33})$$

$$\hat{I} = I_1 + J_1 + I_2 + J_2 \quad (\text{S34})$$

$$(\text{S35})$$

⁵⁴⁵ These quantities are used to compute the normalized distance from the attractor, as
⁵⁴⁶ described in the main text.

⁵⁴⁷ Estimating intrinsic resilience using mechanistic model

⁵⁴⁸ We test whether we can reliably estimate the intrinsic resilience of a system by fitting
⁵⁴⁹ a mechanistic model. Specifically, we simulate case time series from stochastic SIRS
⁵⁵⁰ and two-strain models and fit a simple, deterministic SIRS model using a Bayesian
⁵⁵¹ framework.

⁵⁵² First, we describe the simulation set up. The stochastic SIRS model can be
⁵⁵³ written as follows:

$$\beta(t) = \mathcal{R}_0 \left(1 + \theta \cos \left(\frac{2\pi t}{364} \right) \right) \alpha(t)(1 - \exp(-\gamma)) \quad (\text{S36})$$

$$\text{FOI}(t) = \beta(t)I(t - \Delta t)/N \quad (\text{S37})$$

$$B(t) \sim \text{Poisson}(\mu N) \quad (\text{S38})$$

$$\Delta S(t) \sim \text{Binom}(S(t - \Delta t), 1 - \exp(-(\text{FOI}(t) + \mu)\Delta t)) \quad (\text{S39})$$

$$N_{SI}(t) \sim \text{Binom}\left(\Delta S(t), \frac{\text{FOI}(t)}{\text{FOI}(t) + \mu}\right) \quad (\text{S40})$$

$$\Delta I(t) \sim \text{Binom}(I(t - \Delta t), 1 - \exp(-(\gamma + \mu)\Delta t)) \quad (\text{S41})$$

$$N_{IR}(t) \sim \text{Binom}\left(\Delta I(t), \frac{\gamma}{\gamma + \mu}\right) \quad (\text{S42})$$

$$\Delta R(t) \sim \text{Binom}(R(t - \Delta t), 1 - \exp(-(\delta + \mu)\Delta t)) \quad (\text{S43})$$

$$N_{RS}(t) \sim \text{Binom}\left(\Delta R(t), \frac{\delta}{\delta + \mu}\right) \quad (\text{S44})$$

$$S(t) = S(t - \Delta t) + N_{RS}(t) + B(t) - \Delta S(t) \quad (\text{S45})$$

$$I(t) = I(t - \Delta t) + N_{SI}(t) - \Delta I(t) \quad (\text{S46})$$

$$R(t) = R(t - \Delta t) + N_{IR}(t) - \Delta R(t) \quad (\text{S47})$$

⁵⁵⁴ where FOI represent the force of infection; N_{ij} represent the number of individuals
⁵⁵⁵ moving from compartment i to j on a given day; and $B(t)$ represents the number
⁵⁵⁶ of new births. We simulate the model on a daily scale—assuming 364 days in a
⁵⁵⁷ year so that it can be evenly grouped into 52 weeks—with the following parameters:
⁵⁵⁸ $\mathcal{R}_0 = 3$, $\theta = 0.1$, $\gamma = 1/7/\text{days}$, $\delta = 1/(364 \times 2)/\text{days}$, $\mu = 1/(364 \times 50)/\text{days}$, and

559 $N = 1 \times 10^8$. The model is simulated from 1900 to 2030 assuming $S(0) = N/3$,
560 $I(0) = 100$, and $R(0) = N - S(0) - I(0)$. The observed incidence from the model is
561 then simulated as follows:

$$C(t) = \text{Beta} - \text{Binom}(N_{SI}(t), \rho, k), \quad (\text{S48})$$

562 where ρ represents the reporting probability and k represents the overdispersion pa-
563 rameter of beta-binomial distribution. We assume $\rho = 0.002$ (i.e., 0.2% probability)
564 and $k = 1000$.

565 The stochastic two-strain model can be written as follows:

$$\beta_1(t) = b_1 \left(1 + \theta_1 \cos \left(\frac{2\pi(t - \phi_1)}{364} \right) \right) \alpha(t) \quad (\text{S49})$$

$$\beta_2(t) = b_2 \left(1 + \theta_2 \cos \left(\frac{2\pi(t - \phi_2)}{364} \right) \right) \alpha(t) \quad (\text{S50})$$

$$\text{FOI}_1(t) = \beta_1(t)(I_1(t - \Delta t) + J_1(t - \Delta t))/N \quad (\text{S51})$$

$$\text{FOI}_2(t) = \beta_2(t)(I_2(t - \Delta t) + J_2(t - \Delta t))/N \quad (\text{S52})$$

$$B(t) \sim \text{Poisson}(\mu N) \quad (\text{S53})$$

$$\Delta S(t) \sim \text{Binom}(S(t - \Delta t), 1 - \exp(-(\text{FOI}_1(t) + \text{FOI}_2(t) + \mu)\Delta t)) \quad (\text{S54})$$

$$N_{SI_1}(t) \sim \text{Binom}\left(\Delta S(t), \frac{\text{FOI}_1(t)}{\text{FOI}_1(t) + \text{FOI}_2(t) + \mu}\right) \quad (\text{S55})$$

$$N_{SI_2}(t) \sim \text{Binom}\left(\Delta S(t), \frac{\text{FOI}_2(t)}{\text{FOI}_1(t) + \text{FOI}_2(t) + \mu}\right) \quad (\text{S56})$$

$$\Delta I_1(t) \sim \text{Binom}(I_1(t - \Delta t), 1 - \exp(-(\gamma_1 + \mu)\Delta t)) \quad (\text{S57})$$

$$N_{I_1 R_1}(t) \sim \text{Binom}\left(\Delta I_1(t), \frac{\gamma_1}{\gamma_1 + \mu}\right) \quad (\text{S58})$$

$$\Delta I_2(t) \sim \text{Binom}(I_2(t - \Delta t), 1 - \exp(-(\gamma_2 + \mu)\Delta t)) \quad (\text{S59})$$

$$N_{I_2 R_2}(t) \sim \text{Binom}\left(\Delta I_2(t), \frac{\gamma_2}{\gamma_2 + \mu}\right) \quad (\text{S60})$$

$$\Delta R_1(t) \sim \text{Binom}(R_1(t - \Delta t), 1 - \exp(-(\epsilon_{21}\text{FOI}_2(t) + \rho_1 + \mu)\Delta t)) \quad (\text{S61})$$

$$N_{R_1 S}(t) \sim \text{Binom}\left(\Delta R_1(t), \frac{\rho_1}{\epsilon_{21}\text{FOI}_2(t) + \rho_1 + \mu}\right) \quad (\text{S62})$$

$$N_{R_1 J_2}(t) \sim \text{Binom}\left(\Delta R_1(t), \frac{\epsilon_{21}\text{FOI}_2(t)}{\epsilon_{21}\text{FOI}_2(t) + \rho_1 + \mu}\right) \quad (\text{S63})$$

$$\Delta R_2(t) \sim \text{Binom}(R_2(t - \Delta t), 1 - \exp(-(\epsilon_{12}\text{FOI}_1(t) + \rho_2 + \mu)\Delta t)) \quad (\text{S64})$$

$$N_{R_2 S}(t) \sim \text{Binom}\left(\Delta R_2(t), \frac{\rho_2}{\epsilon_{12}\text{FOI}_1(t) + \rho_2 + \mu}\right) \quad (\text{S65})$$

$$N_{R_2 J_1}(t) \sim \text{Binom}\left(\Delta R_2(t), \frac{\epsilon_{12}\text{FOI}_1(t)}{\epsilon_{12}\text{FOI}_1(t) + \rho_2 + \mu}\right) \quad (\text{S66})$$

$$\Delta J_1(t) \sim \text{Binom}(J_1(t - \Delta t), 1 - \exp(-(\gamma_1 + \mu)\Delta t)) \quad (\text{S67})$$

$$N_{J_1R}(t) \sim \text{Binom}\left(\Delta J_1(t), \frac{\gamma_1}{\gamma_1 + \mu}\right) \quad (\text{S68})$$

$$\Delta J_2(t) \sim \text{Binom}(J_2(t - \Delta t), 1 - \exp(-(\gamma_2 + \mu)\Delta t)) \quad (\text{S69})$$

$$N_{J_2R}(t) \sim \text{Binom}\left(\Delta J_2(t), \frac{\gamma_2}{\gamma_2 + \mu}\right) \quad (\text{S70})$$

$$\Delta R(t) \sim \text{Binom}(R(t - \Delta t), 1 - \exp(-(\rho_1 + \rho_2 + \mu)\Delta t)) \quad (\text{S71})$$

$$N_{RR_1}(t) \sim \text{Binom}\left(\Delta R(t), \frac{\rho_1}{\rho_1 + \rho_2 + \mu}\right) \quad (\text{S72})$$

$$N_{RR_2}(t) \sim \text{Binom}\left(\Delta R(t), \frac{\rho_2}{\rho_1 + \rho_2 + \mu}\right) \quad (\text{S73})$$

$$S(t) = S(t - \Delta t) - \Delta S(t) + B(t) + N_{R_1S}(t) + N_{R_2S}(t) \quad (\text{S74})$$

$$I_1(t) = I_1(t - \Delta t) - \Delta I_1(t) + N_{SI_1}(t) \quad (\text{S75})$$

$$I_2(t) = I_2(t - \Delta t) - \Delta I_2(t) + N_{SI_2}(t) \quad (\text{S76})$$

$$R_1(t) = R_1(t - \Delta t) - \Delta R_1(t) + N_{I_1R_1}(t) + N_{RR_1}(t) \quad (\text{S77})$$

$$R_2(t) = R_2(t - \Delta t) - \Delta R_2(t) + N_{I_2R_2}(t) + N_{RR_2}(t) \quad (\text{S78})$$

$$J_1(t) = J_1(t - \Delta t) - \Delta J_1(t) + N_{R_2J_1}(t) \quad (\text{S79})$$

$$J_2(t) = J_2(t - \Delta t) - \Delta J_2(t) + N_{R_1J_2}(t) \quad (\text{S80})$$

$$R(t) = R(t - \Delta t) - \Delta R(t) + N_{J_1R}(t) + N_{J_2R}(t) \quad (\text{S81})$$

566 We simulate the model on a daily scale with previously estimated parameters for the
 567 RSV-HMPV interaction [19]: $b_1 = 1.7/\text{weeks}$, $b_2 = 1.95/\text{weeks}$, $\theta_1 = 0.4$, $\theta_2 = 0.3$,
 568 $\phi_1 = 0.005 \times 7/364$, $\phi_2 = 4.99 \times 7/364$, $\epsilon_{12} = 0.92$, $\epsilon_{21} = 0.45$, $\gamma_1 = 1/10/\text{days}$,
 569 $\gamma_2 = 1/10/\text{days}$, $\rho_1 = 1/364/\text{days}$, $\rho_2 = 1/364/\text{days}$, $\mu = 1/(70 \times 364)/\text{days}$, and
 570 $N = 1 \times 10^8$. The model is simulated from 1900 to 2030 assuming $S(0) = N - 200$,
 571 $I_1(0) = 100$, $I_2(0) = 100$, $R_1(0) = 0$, $R_2(0) = 0$, $J_1(0) = 0$, $J_2(0) = 0$, and $R(0) = 0$.
 572 The observed incidence for each strain is then simulated as follows:

$$C_1(t) = \text{Beta} - \text{Binom}(N_{SI_1}(t) + N_{R_2J_1}, \rho, k), \quad (\text{S82})$$

$$C_2(t) = \text{Beta} - \text{Binom}(N_{SI_2}(t) + N_{R_1J_2}, \rho, k), \quad (\text{S83})$$

573 where ρ represents the reporting probability and k represents the overdispersion pa-
 574 rameter of beta-binomial distribution. We assume $\rho = 0.002$ (i.e., 0.2% probability)
 575 and $k = 500$. We also consider the total incidence: $C_{\text{total}}(t) = C_1(t) + C_2(t)$.

576 For both models, we consider a more realistic challenges in intervention effects
 577 $\alpha(t)$ to challenge our ability to estimate the intervention effects. Thus, we assume
 578 a 40% transmission reduction for 3 months from March 2020, followed by a 10%
 579 transmission reduction for 6 months, 20% transmission reduction for 3 months, and

580 a final return to normal levels:

$$\alpha(t) = \begin{cases} 1 & t < 2020.25 \\ 0.6 & 2020.25 \leq t < 2020.5 \\ 0.9 & 2020.5 \leq t < 2021 \\ 0.8 & 2021 \leq t < 2021.25 \\ 1 & 2021.25 \leq t \end{cases}. \quad (\text{S84})$$

581 For all simulations, we truncate the time series from the beginning of 2014 to the
582 end of 2023 and aggregate them into weekly cases.

583 To infer intrinsic resilience from time series, we fit a simple discrete time, deter-
584 ministic SIRS model [4]:

$$\Delta t = 1 \text{ week} \quad (\text{S85})$$

$$\text{FOI}(t) = \beta(t)(I(t - \Delta t) + \omega)/N \quad (\text{S86})$$

$$\Delta S(t) = [1 - \exp(-(\text{FOI}(t) + \mu)\Delta t)] S(t - \Delta t) \quad (\text{S87})$$

$$N_{SI}(t) = \frac{\text{FOI}(t)\Delta S(t)}{\text{FOI}(t) + \mu} \quad (\text{S88})$$

$$\Delta I(t) = [1 - \exp(-(\gamma + \mu)\Delta t)] I(t - \Delta t) \quad (\text{S89})$$

$$N_{IR}(t) = \frac{\gamma \Delta I(t)}{\gamma + \mu} \quad (\text{S90})$$

$$\Delta R(t) = [1 - \exp(-(\nu + \mu)\Delta t)] R(t - \Delta t) \quad (\text{S91})$$

$$N_{RS}(t) = \frac{\nu \Delta R(t)}{\nu + \mu} \quad (\text{S92})$$

$$S(t) = S(t - \Delta t) + \mu S - \Delta S(t) + N_{RS}(t) \quad (\text{S93})$$

$$I(t) = I(t - \Delta t) - \Delta I(t) + N_{SI}(t) \quad (\text{S94})$$

$$R(t) = R(t - \Delta t) - \Delta R(t) + N_{IR}(t) \quad (\text{S95})$$

585 where we include an extra term ω to account for external infections. Although actual
586 simulations do not include any external infections, we found that including this term
587 generally helped with model convergence in previous analyses [4]. The transmission
588 rate is divided into a seasonal term $\beta_{\text{seas}}(t)$ (repeated every year) and intervention
589 term $\alpha(t)$, which are estimated jointly:

$$\beta(t) = \beta_{\text{seas}}(t)\alpha(t), \quad (\text{S96})$$

590 where $\alpha < 1$ corresponds to reduction in transmission due to intervention effects. To
591 constrain the smoothness of $\beta_{\text{seas}}(t)$, we impose cyclic, random-walk priors:

$$\beta_{\text{seas}}(t) \sim \text{Normal}(\beta_{\text{seas}}(t - 1), \sigma) \quad t = 2 \dots 52 \quad (\text{S97})$$

$$\beta_{\text{seas}}(1) \sim \text{Normal}(\beta_{\text{seas}}(52), \sigma) \quad (\text{S98})$$

592 [SWP: I noticed that I forgot to put a prior on σ so need to re-do this but won't
 593 change the results.] We fix $\alpha(t) = 1$ for all $t < 2020$ and estimate α assuming a
 594 normal prior:

$$\alpha \sim \text{Normal}(1, 0.25). \quad (\text{S99})$$

595 We assume weakly informative priors on ω and τ :

$$\omega \sim \text{Normal}(0, 200) \tau \sim \text{Normal}(104, 26) \quad (\text{S100})$$

596 We assume that the true birth/death rates, population sizes, and recovery rates are
 597 known. We note, however, that assuming $\gamma = 1/\text{week}$ actually correspond to a
 598 mean infectious period of 1.6 weeks, which is much longer than the true value; this
 599 approximation allows us to test whether we can still robustly estimate the intrinsic
 600 resilience given parameters mis-specification. Initial conditions are estimated with
 601 following priors:

$$S(0) = Ns(0) \quad (\text{S101})$$

$$I(0) = Ni(0) \quad (\text{S102})$$

$$s(0) \sim \text{Uniform}(0, 1) \quad (\text{S103})$$

$$i(0) \sim \text{Half-Normal}(0, 0.001) \quad (\text{S104})$$

602 Finally, the Observation model is specified as follows:

$$\text{Cases}(t) \sim \text{Negative-Binomial}(\rho N_{SI}(t), \phi) \quad (\text{S105})$$

$$\rho \sim \text{Half-Normal}(0, 0.02) \quad (\text{S106})$$

$$\phi \sim \text{Half-Normal}(0, 10) \quad (\text{S107})$$

603 where ρ represents the reporting probability and ϕ represents the negative binomial
 604 overdispersion parameter.

605 The model is fitted to four separate time series: (1) incidence time series from
 606 the SIRS model, (2) incidence time series for strain 1 from the two-strain model,
 607 (3) incidence time series for strain 2 from the two-strain model, and (4) combined
 608 incidence time series for strains 1 and 2 from the two-strain model. The model was
 609 fitted using rstan [26, 27]. The resulting posterior distribution was used to calculate
 610 the intrinsic resilience of the seasonally unforced system with the same parameters;
 611 eigenvalues of the discrete-time SIR model were computed by numerically finding
 612 the equilibrium and calculating the Jacobian matrix.

613 **Validations for window-selection criteria**

614 We use stochastic SIRS simulations to validate the window-selection criteria that we
 615 use for the linear regression for estimating empirical resilience. For each simulation,
 616 we begin by generating a random intervention $\alpha(t)$ from random set of parameters.
 617 First, we draw the duration of intervention τ_{np}^* from a uniform distribution between

618 0.5 and 3.5 years. Then, we draw independent normal variables z_i of length $\lfloor 364\tau_{\text{npi}} \rfloor$
 619 with a standard deviation of 0.02 and take a reverse cumulative sum to obtain a
 620 realistic shape for the intervention:

$$x_n = 1 + \sum_{i=n}^{\lfloor 364\tau_{\text{npi}} \rfloor} z_i, \quad n = 1, \dots, \lfloor 364\tau_{\text{npi}} \rfloor. \quad (\text{S108})$$

621 We repeat this random generation process until less than 10% of x_n exceeds 1. Then,
 622 we set any values that are above 1 or below 0 as 1 and 0, respectively. Then, we
 623 randomly draw the minimum transmission during intervention α_{\min} from a uniform
 624 distribution between 0.5 and 0.7 and scale x_n to have a minimum of α_{\min} :

$$x_{\text{scale},n} = \alpha_{\min} + (1 - \alpha_{\min}) \times \frac{x_n - \min x_n}{1 - \min x_n}. \quad (\text{S109})$$

625 This allows us to simulate a realistically shaped interventions:

$$\alpha(t) = \begin{cases} 1 & t < 2020 \\ x_{\text{scale},364(t-2020)} & 2020 \leq t < 2020 + \tau_{\text{npi}} \\ 1 & \tau_{\text{npi}} \leq t \end{cases}. \quad (\text{S110})$$

626 Given this intervention function, we draw \mathcal{R}_0 from a uniform distribution between 1.5
 627 and 3 and the mean duration of immunity $1/\delta$ from a uniform distribution between
 628 0.5 and 2. Then, we simulate the stochastic SIRS model from $S(0) = 10^8/\mathcal{R}_0$ and
 629 $I(0) = 100$ from 1990 to 2025 and truncate the time series to 2014–2025; if the
 630 epidemic becomes extinct before the end of simulation, we discard that simulation
 631 and start over from the intervention generation step. We then apply the window
 632 selection criteria described in the main text to compute the empirical resilience and
 633 compare it against the intrinsic resilience of the seasonally unforced system. We also
 634 compare this with the naive approach that uses the entire distance-from-attractor
 635 time series, starting from the maximum distance. We repeat this procedure 500
 636 times and quantify the correlation between empirical and intrinsic resilience estimates
 637 across two approaches.

Supplementary Figures

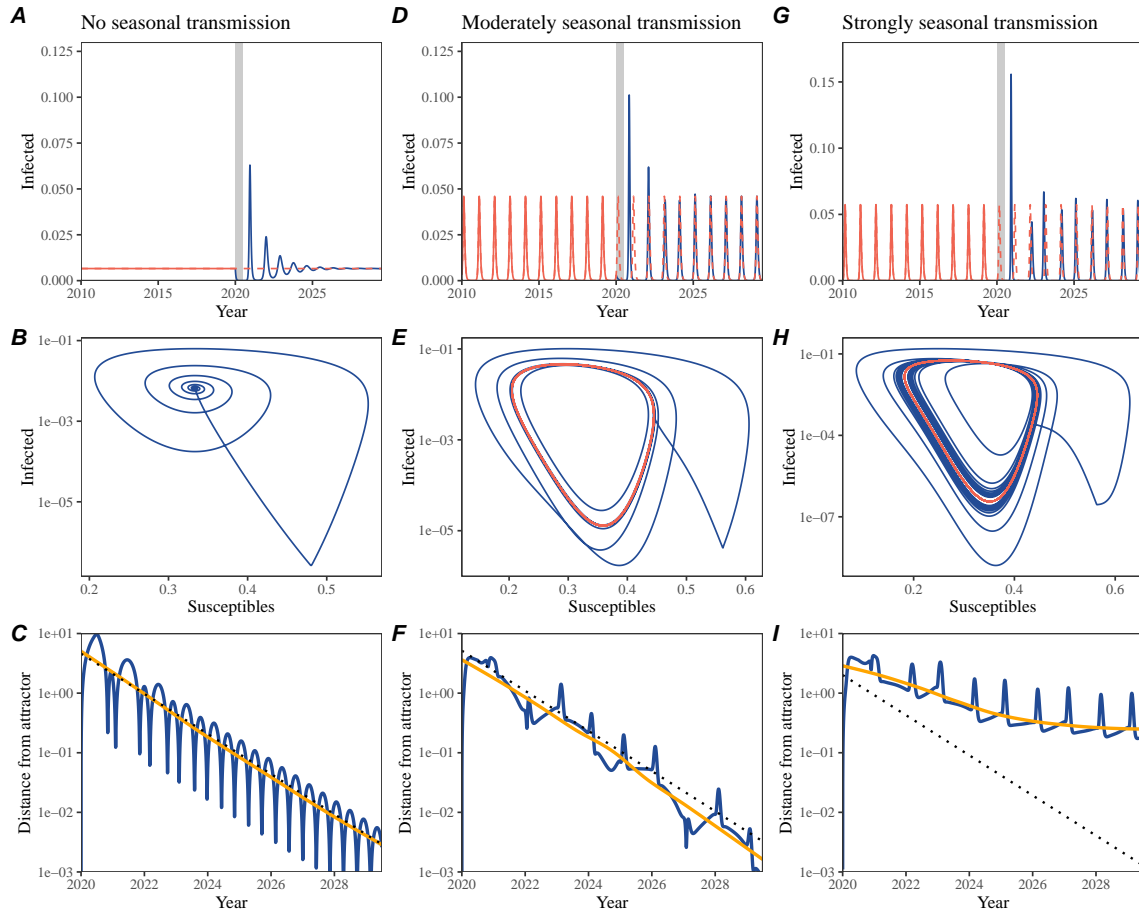


Figure S1: Impact of seasonal transmission on pathogen resilience. (A, D, G) Simulated epidemic trajectories using the SIRS model without seasonal forcing (A), with seasonal forcing of amplitude of 0.2 (D), and with seasonal forcing of amplitude of 0.2 (G). Red and blue solid lines represent epidemic dynamics before and after interventions are introduced, respectively. Red dashed lines represent counterfactual epidemic dynamics in the absence of interventions. Gray regions indicate the duration of interventions. (B, E, H) Phase plane representation of the corresponding model. Red and blue solid lines represent epidemic trajectories on an SI phase plane before and after interventions are introduced, respectively. (C, F, I) Changes in logged distance from attractor over time. Blue lines represent the logged distance from attractor. Orange lines represent the locally estimated scatterplot smoothing (LOESS) fits to the logged distance from attractor. Dotted lines are superimposed as a comparison to have the same slope as the intrinsic resilience of the seasonally unforced system.

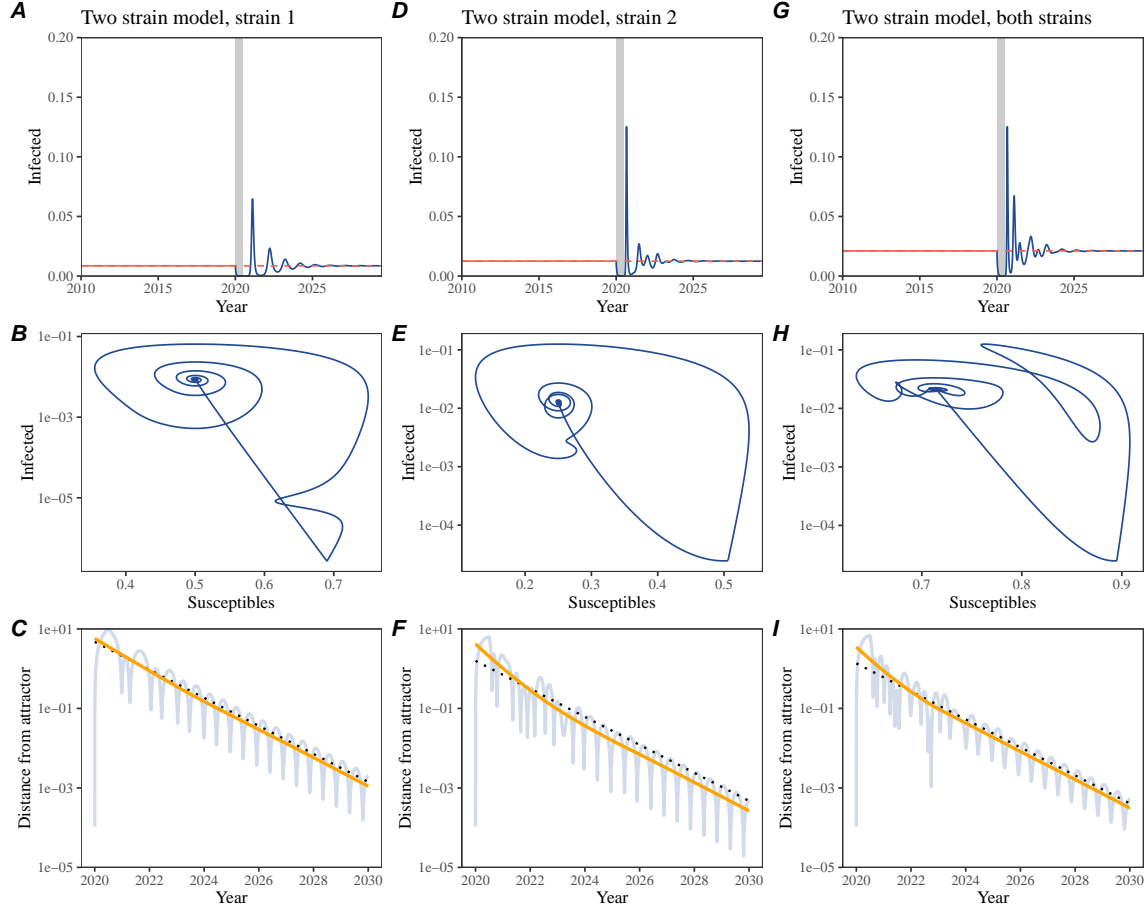


Figure S2: Conceptual framework for measuring pathogen resilience following NPIs for a multi-strain system without seasonal forcing. (A, D, G) Simulated epidemic trajectories using a multi-strain system without seasonal forcing. Red and blue solid lines represent epidemic dynamics before and after interventions are introduced, respectively. Red dashed lines represent counterfactual epidemic dynamics in the absence of interventions. Gray regions indicate the duration of interventions. (B, E, H) Phase plane representation of the corresponding model. Red and blue solid lines represent epidemic trajectories on an SI phase plane before and after interventions are introduced, respectively. (C, F, I) Changes in logged distance from attractor over time. Blue lines represent the logged distance from attractor. Orange lines represent the locally estimated scatterplot smoothing (LOESS) fits to the logged distance from attractor. Dotted lines are superimposed as a comparison to have the same slope as the intrinsic resilience of the seasonally unforced system.

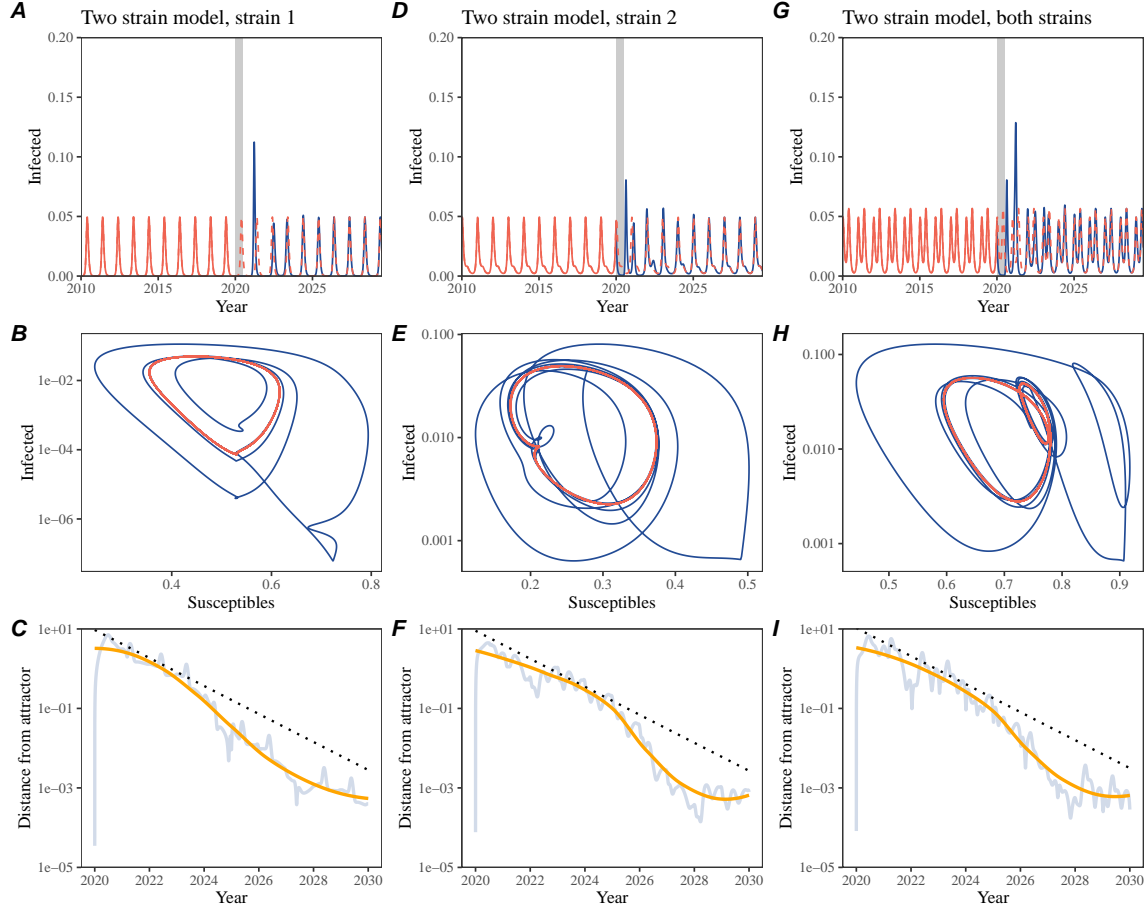


Figure S3: Conceptual framework for measuring pathogen resilience following NPIs for a multi-strain system with seasonal forcing. (A, D, G) Simulated epidemic trajectories using a multi-strain system with seasonal forcing (amplitude of 0.2). Red and blue solid lines represent epidemic dynamics before and after interventions are introduced, respectively. Red dashed lines represent counterfactual epidemic dynamics in the absence of interventions. Gray regions indicate the duration of interventions. (B, E, H) Phase plane representation of the corresponding model. Red and blue solid lines represent epidemic trajectories on an SI phase plane before and after interventions are introduced, respectively. (C, F, I) Changes in logged distance from attractor over time. Blue lines represent the logged distance from attractor. Orange lines represent the locally estimated scatterplot smoothing (LOESS) fits to the logged distance from attractor. Dotted lines are superimposed as a comparison to have the same slope as the intrinsic resilience of the seasonally unforced system.

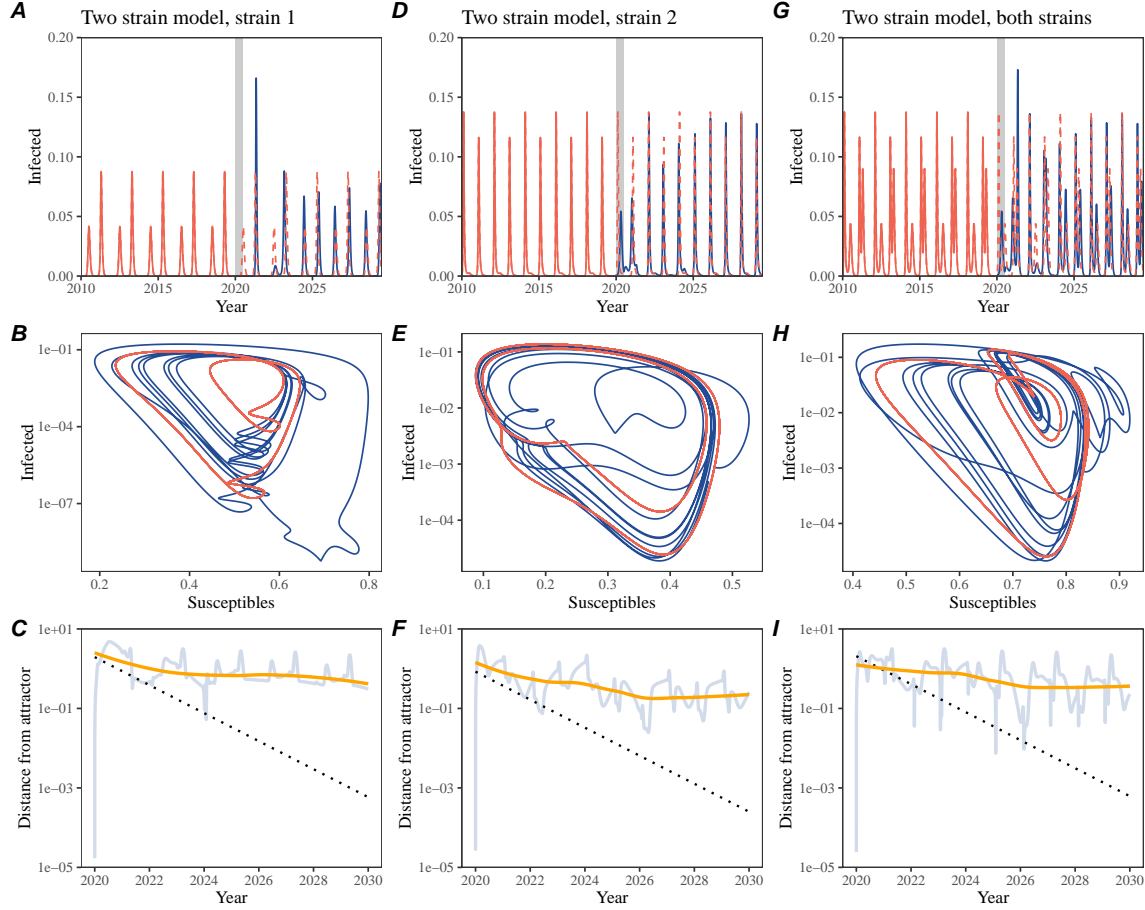


Figure S4: Conceptual framework for measuring pathogen resilience following NPIs for a multi-strain system with strong seasonal forcing. (A, D, G) Simulated epidemic trajectories using a multi-strain system with seasonal forcing (amplitude of 0.4). Red and blue solid lines represent epidemic dynamics before and after interventions are introduced, respectively. Red dashed lines represent counterfactual epidemic dynamics in the absence of interventions. Gray regions indicate the duration of interventions. (B, E, H) Phase plane representation of the corresponding model. Red and blue solid lines represent epidemic trajectories on an SI phase plane before and after interventions are introduced, respectively. (C, F, I) Changes in logged distance from attractor over time. Blue lines represent the logged distance from attractor. Orange lines represent the locally estimated scatterplot smoothing (LOESS) fits to the logged distance from attractor. Dotted lines are superimposed as a comparison to have the same slope as the intrinsic resilience of the seasonally unforced system.

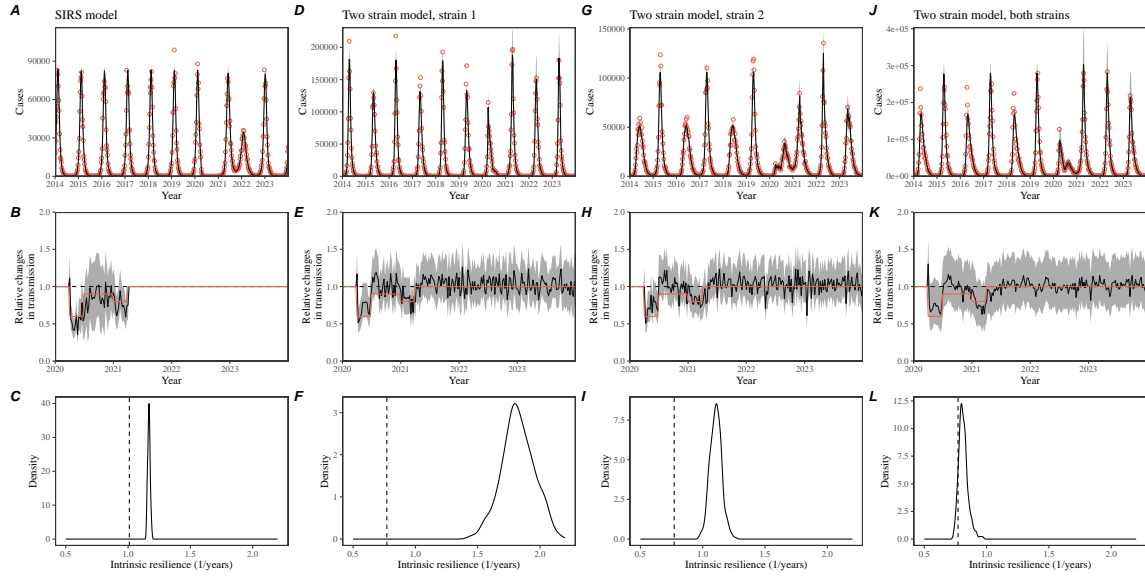


Figure S5: Mechanistic model fits to simulated data and inferred intrinsic resilience. (A, D, G, J) Simulated case time series from corresponding models (red) and SIRS model fits (black). (B, E, H, K) Assumed changes in transmission due to COVID-19 interventions (red) and estimated changes from the SIRS model (black). Solid lines and shaded regions represent fitted posterior median and 95% credible intervals. (C, F, I, L) True intrinsic resilience of the seasonally unforced system (vertical lines) and the posterior distribution of the inferred intrinsic resilience from the SIRS model (density plots).

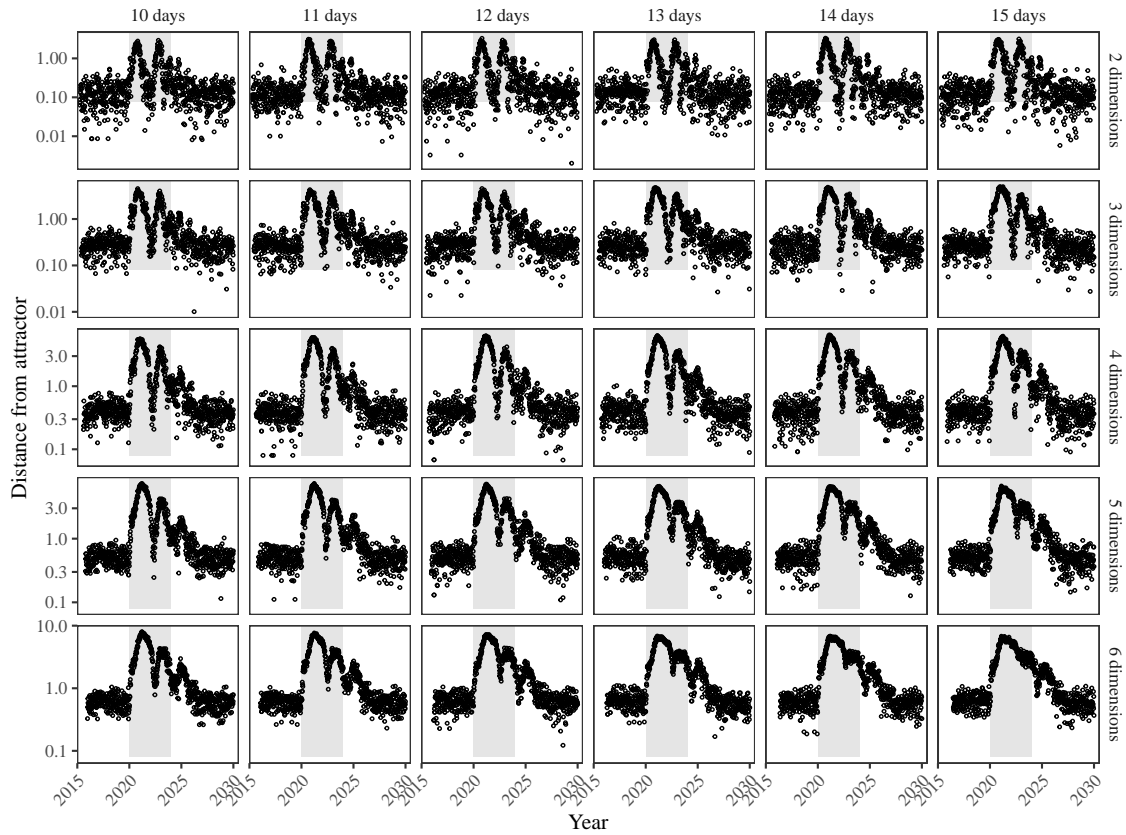


Figure S6: Sensitivity of the distance from attractor to choices about embedding lags and dimensions. Sensitivity analysis for the distance-from-attractor time series shown in Figure 3E in the main text by varying the embedding lag between 10–15 days and embedding dimensions between 2–6 dimensions.

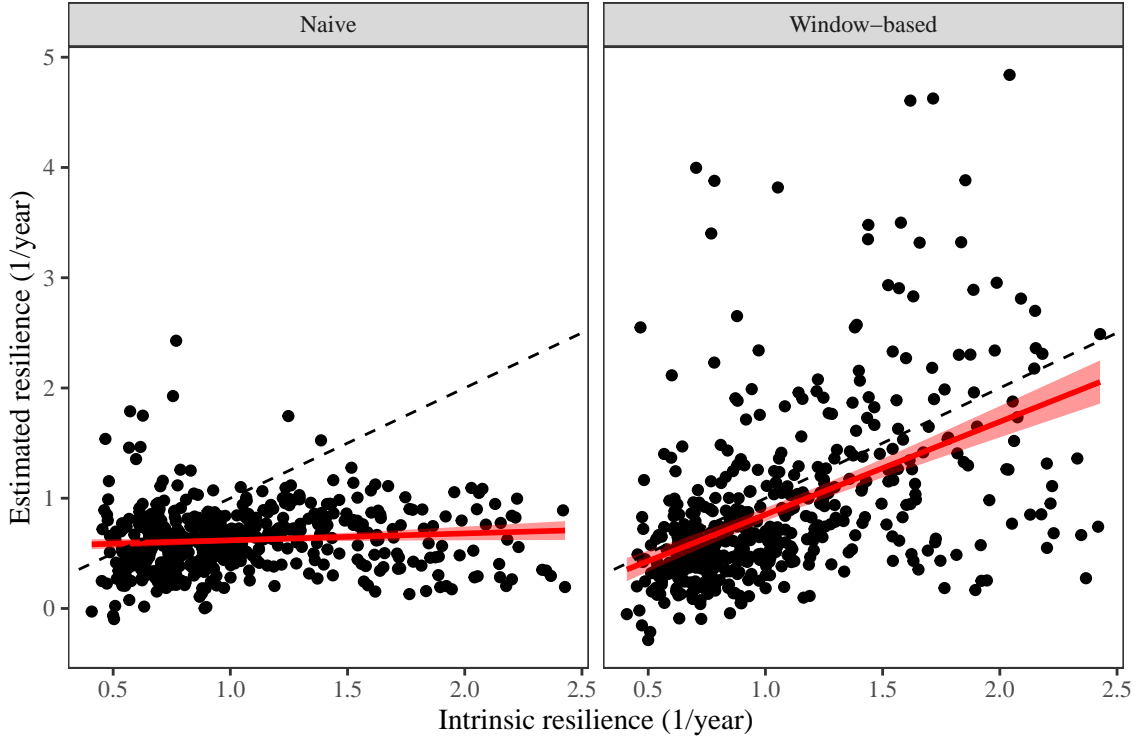


Figure S7: Impact of fitting window selection on the estimation of empirical resilience. We simulate 500 epidemics using stochastic SIRS model with randomly drawn parameters and randomly generated intervention impacts. For each simulation, we reconstruct the empirical attractor based on the approach outlined in Figure 3 and estimate the distance from attractor. The naive approach fits a linear regression on a log scale, starting from the maximum distance until the end of the time series. The window-based approach tries to select an appropriate window by smoothing the distance estimates and finding a time period when the smoothed time series crosses pre-determined threshold, relatively to the maximum distance; then, a linear regression is fitted by using the raw distance within this time period.

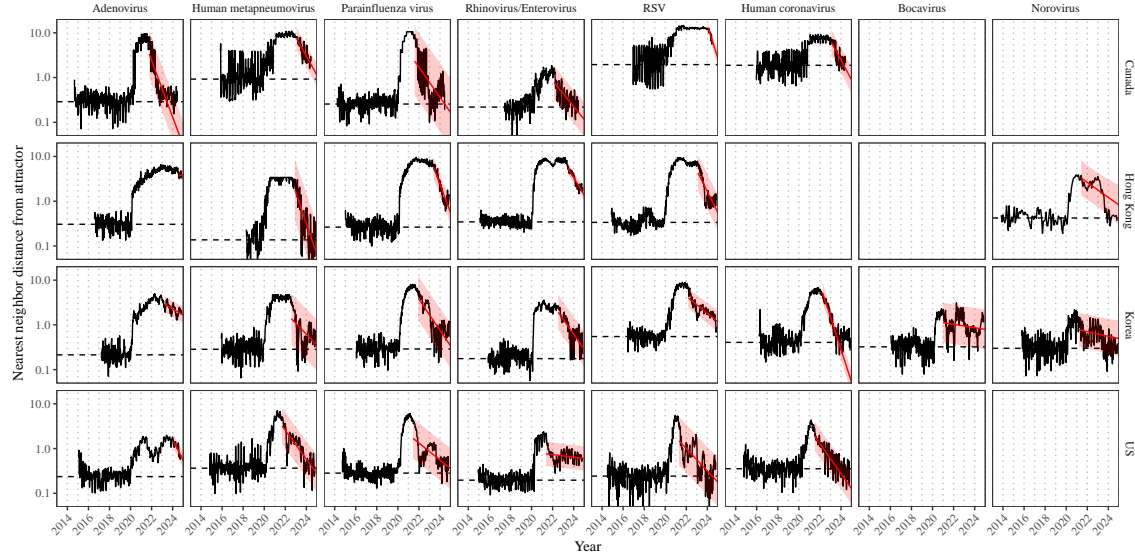


Figure S8: Estimated time series of distance from attractor for each pathogen across Canada, Hong Kong, Korea, and the US. Black lines represent the estimated distance from attractor. Red lines and shaded regions represent the linear regression fits and corresponding 95% confidence intervals. Dashed lines represent the average of the pre-pandemic nearest neighbor distances.

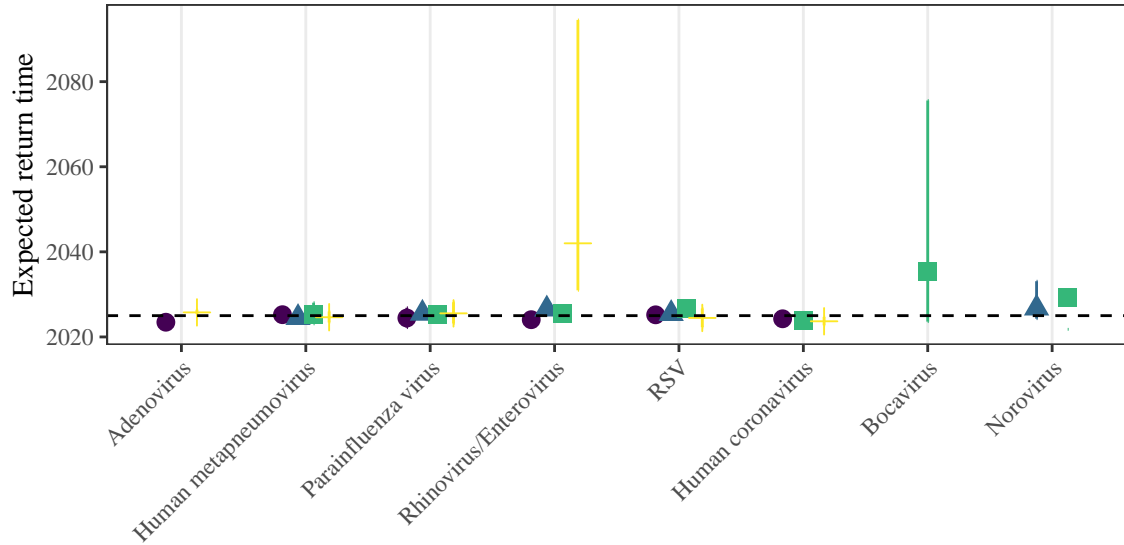


Figure S9: **Predicted timing of when each pathogen will return to their pre-pandemic cycles (zoomed out).** The dashed line in panel B indicates the end of 2024 (current observation time). Error bars represent 95% confidence intervals.

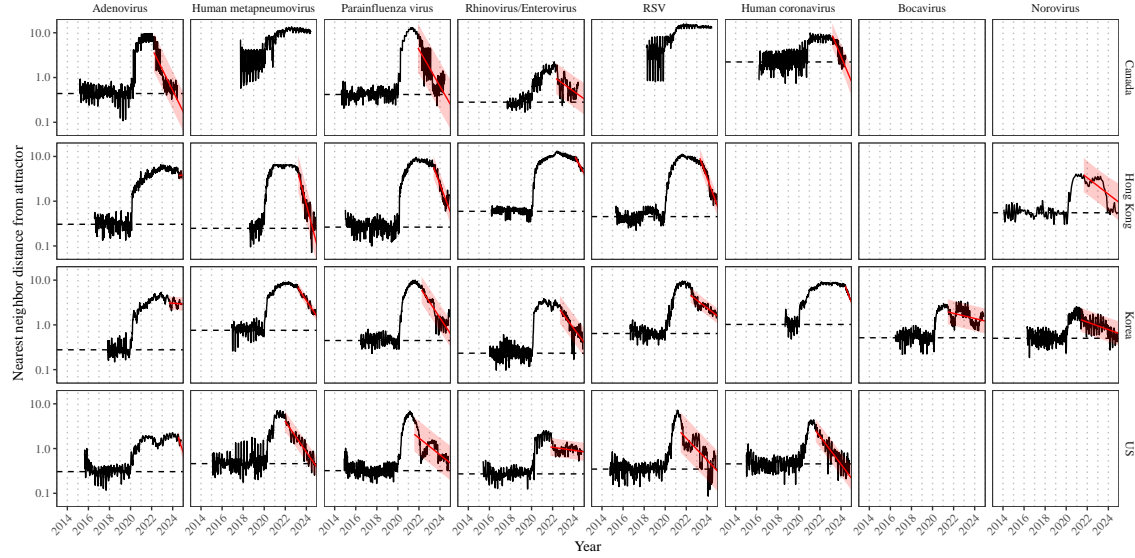


Figure S10: Estimated time series of distance from attractor for each pathogen across Canada, Hong Kong, Korea, and the US using higher embedding dimensions. Black lines represent the estimated distance from attractor. Red lines and shaded regions represent the linear regression fits and corresponding 95% confidence intervals. Dashed lines represent the average of the pre-pandemic nearest neighbor distances. A lower threshold is used for determining embedding dimensions with the false nearest neighbors approach, thereby yielding a higher embedding dimension.

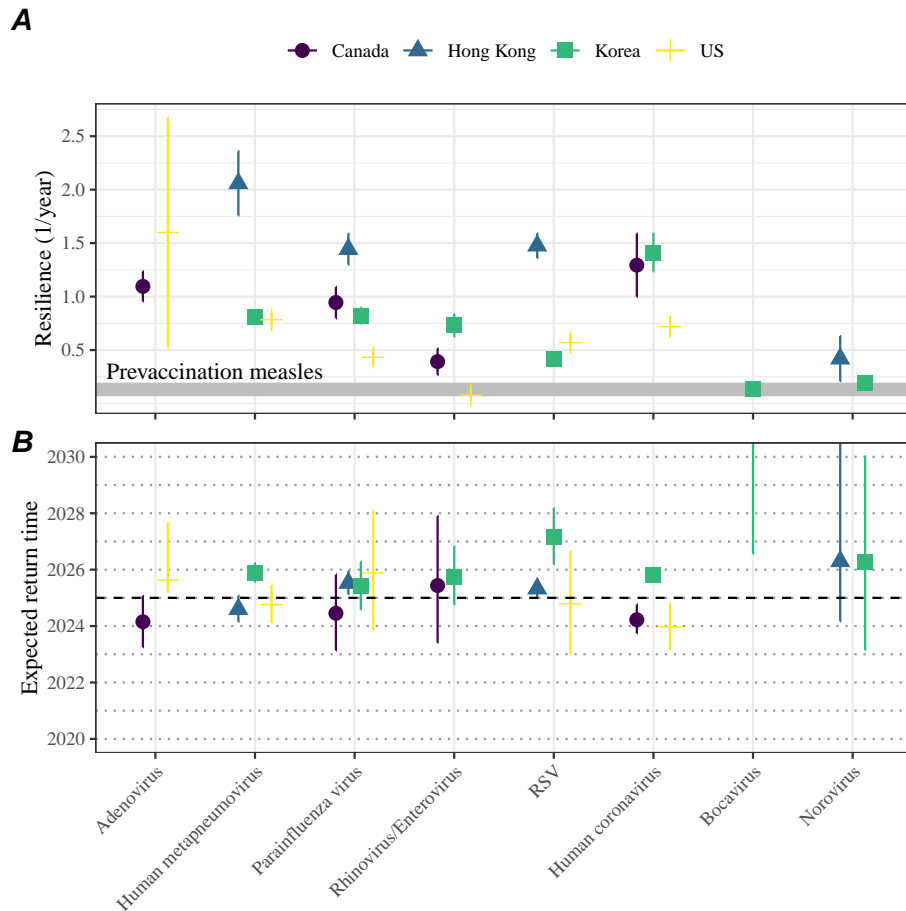


Figure S11: Summary of resilience estimates using higher embedding dimensions. (A) Estimated pathogen resilience. The gray horizontal line represents the intrinsic resilience of pre-vaccination measles dynamics. (B) Predicted timing of when each pathogen will return to their pre-pandemic cycles. The dashed line in panel B indicates the end of 2024 (current observation time). Error bars represent 95% confidence intervals. A lower threshold is used for determining embedding dimensions with the false nearest neighbors approach, thereby yielding a higher embedding dimension.

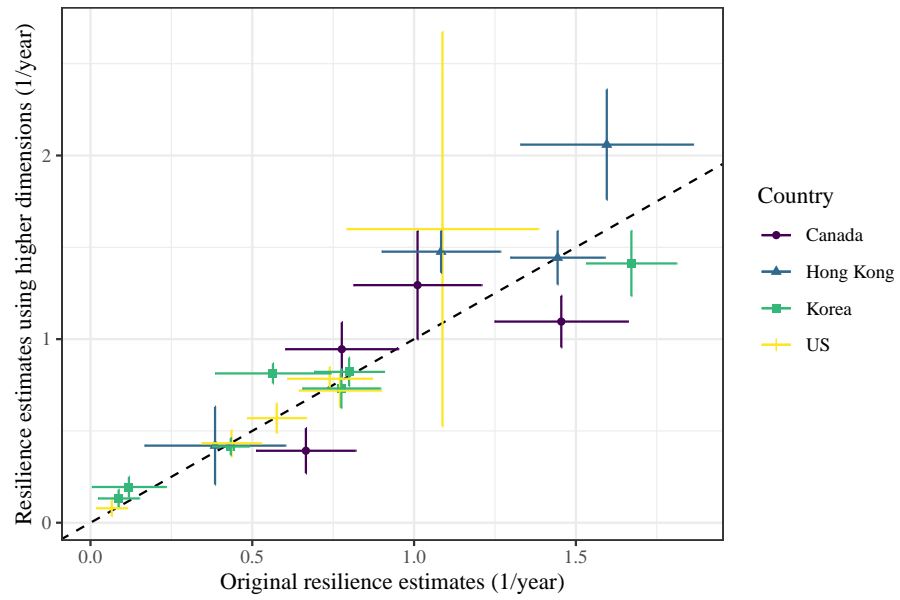


Figure S12: **Comparison of resilience estimates.** Each point represents a resilience estimate for a specific pathogen at a specific country. The x values represent the original resilience estimates presented in Figure 4. The y values represent the original resilience estimates presented in Supplementary Figure S11.

639 References

- 640 [1] Rachel E Baker, Sang Woo Park, Wenchang Yang, Gabriel A Vecchi, C Jessica E
641 Metcalf, and Bryan T Grenfell. The impact of COVID-19 nonpharmaceutical
642 interventions on the future dynamics of endemic infections. *Proceedings of the*
643 *National Academy of Sciences*, 117(48):30547–30553, 2020.
- 644 [2] Gabriela B Gomez, Cedric Mahé, and Sandra S Chaves. Uncertain effects of the
645 pandemic on respiratory viruses. *Science*, 372(6546):1043–1044, 2021.
- 646 [3] Mihaly Koltai, Fabienne Krauer, David Hodgson, Edwin van Leeuwen, Marina
647 Treskova-Schwarzbach, Mark Jit, and Stefan Flasche. Determinants of RSV
648 epidemiology following suppression through pandemic contact restrictions. *Epi-*
649 *demics*, 40:100614, 2022.
- 650 [4] Sang Woo Park, Brooklyn Noble, Emily Howerton, Bjarke F Nielsen, Sarah
651 Lentz, Lilliam Ambroggio, Samuel Dominguez, Kevin Messacar, and Bryan T
652 Grenfell. Predicting the impact of non-pharmaceutical interventions against
653 COVID-19 on *Mycoplasma pneumoniae* in the United States. *Epidemics*,
654 49:100808, 2024.
- 655 [5] Amanda C Perofsky, Chelsea L Hansen, Roy Burstein, Shanda Boyle, Robin
656 Prentice, Cooper Marshall, David Reinhart, Ben Capodanno, Melissa Truong,
657 Kristen Schwabe-Fry, et al. Impacts of human mobility on the citywide trans-
658 mission dynamics of 18 respiratory viruses in pre-and post-COVID-19 pandemic
659 years. *Nature communications*, 15(1):4164, 2024.
- 660 [6] Eric J Chow, Timothy M Uyeki, and Helen Y Chu. The effects of the COVID-19
661 pandemic on community respiratory virus activity. *Nature Reviews Microbiol-*
662 *ogy*, 21(3):195–210, 2023.
- 663 [7] Stephen M Kissler, Christine Tedijanto, Edward Goldstein, Yonatan H Grad,
664 and Marc Lipsitch. Projecting the transmission dynamics of SARS-CoV-2
665 through the postpandemic period. *Science*, 368(6493):860–868, 2020.
- 666 [8] Rachel E Baker, Chadi M Saad-Roy, Sang Woo Park, Jeremy Farrar, C Jessica E
667 Metcalf, and Bryan T Grenfell. Long-term benefits of nonpharmaceutical inter-
668 ventions for endemic infections are shaped by respiratory pathogen dynamics.
669 *Proceedings of the National Academy of Sciences*, 119(49):e2208895119, 2022.
- 670 [9] John-Sebastian Eden, Chisha Sikazwe, Ruopeng Xie, Yi-Mo Deng, Sheena G
671 Sullivan, Alice Michie, Avram Levy, Elena Cutmore, Christopher C Blyth,
672 Philip N Britton, et al. Off-season RSV epidemics in Australia after easing
673 of COVID-19 restrictions. *Nature communications*, 13(1):2884, 2022.
- 674 [10] Stuart L Pimm. The structure of food webs. *Theoretical population biology*,
675 16(2):144–158, 1979.

- 676 [11] Michael G Neubert and Hal Caswell. Alternatives to resilience for measuring
677 the responses of ecological systems to perturbations. *Ecology*, 78(3):653–665,
678 1997.
- 679 [12] Lance H Gunderson. Ecological resilience—in theory and application. *Annual
680 review of ecology and systematics*, 31(1):425–439, 2000.
- 681 [13] Vasilis Dakos and Sonia Kéfi. Ecological resilience: what to measure and how.
682 *Environmental Research Letters*, 17(4):043003, 2022.
- 683 [14] Floris Takens. Detecting strange attractors in turbulence. In *Dynamical Sys-
684 tems and Turbulence, Warwick 1980: proceedings of a symposium held at the
685 University of Warwick 1979/80*, pages 366–381. Springer, 2006.
- 686 [15] Jonathan Dushoff, Joshua B Plotkin, Simon A Levin, and David JD Earn. Dynamical resonance can account for seasonality of influenza epidemics. *Pro-
687 ceedings of the National Academy of Sciences*, 101(48):16915–16916, 2004.
- 688 [16] Alan Hastings, Karen C Abbott, Kim Cuddington, Tessa Francis, Gabriel Gell-
689 ner, Ying-Cheng Lai, Andrew Morozov, Sergei Petrovskii, Katherine Scran-
690 ton, and Mary Lou Zeeman. Transient phenomena in ecology. *Science*,
691 361(6406):eaat6412, 2018.
- 692 [17] Matthew B Kennel, Reggie Brown, and Henry DI Abarbanel. Determining
693 embedding dimension for phase-space reconstruction using a geometrical con-
694 struction. *Physical review A*, 45(6):3403, 1992.
- 695 [18] Eugene Tan, Shannon Algar, Débora Corrêa, Michael Small, Thomas Stemler,
696 and David Walker. Selecting embedding delays: An overview of embedding
697 techniques and a new method using persistent homology. *Chaos: An Interdis-
698 ciplinary Journal of Nonlinear Science*, 33(3), 2023.
- 699 [19] Samit Bhattacharyya, Per H Gesteland, Kent Korgenski, Ottar N Bjørnstad,
700 and Frederick R Adler. Cross-immunity between strains explains the dynamical
701 pattern of paramyxoviruses. *Proceedings of the National Academy of Sciences*,
702 112(43):13396–13400, 2015.
- 703 [20] Bryan T Grenfell, Ottar N Bjørnstad, and Bärbel F Finkenstädt. Dynamics of
704 measles epidemics: scaling noise, determinism, and predictability with the TSIR
705 model. *Ecological monographs*, 72(2):185–202, 2002.
- 706 [21] Virginia E Pitzer, Cécile Viboud, Vladimir J Alonso, Tanya Wilcox, C Jessica
707 Metcalf, Claudia A Steiner, Amber K Haynes, and Bryan T Grenfell. Environ-
708 mental drivers of the spatiotemporal dynamics of respiratory syncytial virus in
709 the United States. *PLoS pathogens*, 11(1):e1004591, 2015.

- 711 [22] Katharine R Dean, Fabienne Krauer, Lars Walløe, Ole Christian Lingjærde, Bar-
712 bara Bramanti, Nils Chr Stenseth, and Boris V Schmid. Human ectoparasites
713 and the spread of plague in Europe during the Second Pandemic. *Proceedings*
714 *of the National Academy of Sciences*, 115(6):1304–1309, 2018.
- 715 [23] Margarita Pons-Salort and Nicholas C Grassly. Serotype-specific immunity
716 explains the incidence of diseases caused by human enteroviruses. *Science*,
717 361(6404):800–803, 2018.
- 718 [24] Sarah Cobey and Edward B Baskerville. Limits to causal inference with state-
719 space reconstruction for infectious disease. *PloS one*, 11(12):e0169050, 2016.
- 720 [25] Edward Goldstein, Sarah Cobey, Saki Takahashi, Joel C Miller, and Marc Lip-
721 sitch. Predicting the epidemic sizes of influenza A/H1N1, A/H3N2, and B: a
722 statistical method. *PLoS medicine*, 8(7):e1001051, 2011.
- 723 [26] Bob Carpenter, Andrew Gelman, Matthew D Hoffman, Daniel Lee, Ben
724 Goodrich, Michael Betancourt, Marcus A Brubaker, Jiqiang Guo, Peter Li,
725 and Allen Riddell. Stan: A probabilistic programming language. *Journal of*
726 *statistical software*, 76, 2017.
- 727 [27] Stan Development Team. RStan: the R interface to Stan, 2024. R package
728 version 2.32.6.